

Seasonal temperatures in West Antarctica during the Holocene

Tyler R. Jones^{1*}, Kurt M. Cuffey², William H. G. Roberts³, Bradley R. Markle^{1,4}, Eric J. Steig⁵, C. Max Stevens^{6,7}, Paul J. Valdes⁸, T. J. Fudge⁵, Michael Sigl⁹, Abigail G. Hughes^{1,4}, Valerie Morris¹, Bruce H. Vaughn¹, Joshua Garland¹⁰, Bo M. Vinther¹¹, Kevin S. Rozmiarek^{1,4}, Chloe A. Brashear^{1,4}, James W. C. White¹²

¹ Institute of Arctic and Alpine Research, University of Colorado, Boulder, CO, USA

² Department of Geography, University of California, Berkeley, CA, USA

³ Geography and Environmental Sciences, Northumbria University, Newcastle, UK

⁴ Department of Geological Sciences, University of Colorado, Boulder, CO, USA

⁵ Department of Earth and Space Sciences, University of Washington, Seattle, WA, USA

⁶ Cryospheric Science Laboratory, NASA Goddard Space Flight Center, Greenbelt, MD, USA

⁷ Earth System Science Interdisciplinary Center, University of Maryland, College Park, MD, USA

⁸ School of Geographical Sciences, University of Bristol, Bristol, UK

⁹ Climate and Environmental Physics, Physics Institute & Oeschger Centre for Climate Change Research, University of Bern, Bern, Switzerland

¹⁰ Center on Narrative, Disinformation and Strategic Influence, Arizona State University, Tempe, AZ, USA

¹¹ Centre for Ice and Climate, Niels Bohr Institute, University of Copenhagen, Denmark

¹² College of Arts and Sciences, University of North Carolina, Chapel Hill, NC, USA

*corresponding author: Tyler Jones (tyler.jones@colorado.edu)

24 **The recovery of long-term climate proxy records with seasonal resolution is rare because of natural smoothing**
25 **processes, discontinuities, and limitations in measurement resolution. Yet insolation forcing, a primary driver**
26 **of multi-millennial-scale climate change, acts through seasonal variations with direct impacts on seasonal**
27 **climate¹. Whether the sensitivity of seasonal climate to insolation matches theoretical predictions has not been**
28 **assessed over long timescales. Here, we analyze a continuous record of water-isotope ratios from the West**
29 **Antarctic Ice Sheet (WAIS) Divide ice core to reveal summer and winter temperature changes through the last**
30 **11,000 years. Summer temperatures in West Antarctica increased through the early-to-mid Holocene, reached**
31 **a peak at 4.1 ka, and then decreased to the present. Climate model simulations show that these variations**
32 **primarily reflect changes in maximum summer insolation, confirming the general connection between seasonal**
33 **insolation and warming, and demonstrating the importance of insolation intensity rather than seasonally**
34 **integrated insolation or season duration^{2,3}. Winter temperatures varied less overall, consistent with predictions**
35 **from insolation forcing, but also fluctuated in the early Holocene, likely owing to changes in meridional heat**
36 **transport. The magnitudes of summer and winter temperature changes constrain the lowering of the WAIS**
37 **surface since the early Holocene to less than 162 m, and most likely less than 58 m, consistent with geological**
38 **constraints elsewhere in West Antarctica^{4,5,6,7}.**

39
40 Milankovitch famously postulated that variations of Earth's orbit and axis drive climate changes over tens of thousands
41 of years by altering the seasonal cycle of insolation¹. By controlling summer temperatures and ice ablation, summer
42 insolation in the northern high latitudes is thought to drive global ice volume changes over glacial-interglacial
43 timescales⁸. While modeling studies support this idea^{9,10}, empirical evidence of the specific climate response to
44 insolation changes derives almost entirely from mean-annual temperature reconstructions^{11,12} or from indirect effects
45 on, for example, trapped gases and melt layers in polar ice^{13,14} and marine eolian deposits¹⁵. The absence of seasonal
46 temperature reconstructions has precluded direct evidence of insolation forcing on seasonal climate, a relationship that
47 may vary geographically. In Antarctica, long records of multiple glacial-interglacial cycles have supported different
48 claims about whether summer insolation's effects relate most strongly to its maximum intensity, its seasonal integral,
49 or to duration above a threshold^{2,3,16,17}. Site-specific empirical determinations would provide valuable tests of such
50 competing ideas.

51
52 **Seasonal Temperature Reconstructions**
53 We reconstructed seasonal temperature variability in West Antarctica through the Holocene (the last 11,000 years)
54 and performed new model experiments to understand its physical controls. The Holocene offers a window of time for
55 assessing the influence of orbital forcing without the complicating effects of Northern Hemisphere deglaciation¹⁸. Our
56 reconstruction (Figures 1,2) uses the high-resolution water isotope record from the WAIS Divide ice core (WDC)^{18,19,20}
57 (Methods Section 1, ED Figure 1a,b), obtained with a continuous-flow technique that provides millimeter-scale depth
58 resolution²¹. Layer ages were determined previously^{2,22}.

59

60 Records of seasonal temperatures from ice cores are limited by measurement resolution and information loss from
61 water-isotope diffusion. In Greenland, the longest records separating summer and winter variability extend to only 2
62 ka^{23,24}, while only climate model simulations are available for older periods¹⁰. For Antarctica, prior to the present
63 study, the longest records spanned only a few centuries²⁵. A combination of three factors account for the considerably
64 greater scope of our reconstruction: exceptional depth resolution of measurements, conditions at WAIS Divide (high
65 accumulation, low temperature, thick ice) that allow for preservation of sub-annual information through the entire
66 Holocene²⁶, and an analysis strategy that circumvents interannual noise by evaluating millennial averages of the
67 seasonal parameters.

68
69 Our method corrects water-isotope variations for diffusion^{26,27,28} and assesses uncertainties including preservation bias
70 and precipitation intermittency (Methods Sections 2 and 3). The diffusion correction operates on the high-resolution
71 data and produces isotopic time-series from which seasonal summer-winter amplitudes were extracted. These were
72 converted to temperature using a model-derived scaling²⁹ (6.96 per mil $\delta D/^\circ C$; Methods Section 2.2) and added to
73 previously reconstructed annual-mean temperatures³⁰ to obtain summer and winter histories.

74 75 **Seasonal Trends**

76 Summer temperatures at WAIS Divide (Figure 2a) generally rose through the early and middle Holocene, persisted at
77 a maximum between ~ 5 and 1.5 ka, then decreased toward the present, with a total Holocene range of around $2^\circ C$.
78 These variations broadly correlate with local maximum insolation, rather than with integrated summer insolation or
79 the duration of summer (Figure 3d,e). Winter temperatures varied less than summer ones overall ($\sim 1^\circ C$ range), but
80 also fluctuated at ~ 10 to 8 ka, a variation too rapid to attribute to orbital forcing.

81
82 Annual mean WAIS Divide temperature changes³⁰ (Figure 2e) were considerably influenced by winter variability in
83 the early Holocene, whereas summer variability dominates the overall Holocene pattern (Methods Section 3.4, ED
84 Table 2). Summer variability also accounts for most of the cooling in the last 2 kyr, indicating that the $\sim 1^\circ C$ annual-
85 average cooling of the entire West Antarctic during this period^{31,32} likewise reflects this season. Neither season at
86 WDC experienced the early Holocene optimum nor overall Holocene cooling that appears in some global temperature
87 reconstructions^{33,34}. To assess the significance of the dominant multi-millennial trends in each season, we performed
88 Monte Carlo analysis (Methods Section 3.5) using 4 ka as a demarcation point in summer (this is the timing of
89 maximum summer temperature) and 6 ka in winter (when winter temperatures plateau). For summer (Figure 2b) this
90 indicates a $>95\%$ chance that warming from 11 to 4 ka and cooling from 4 ka to present exceeded $0.7^\circ C$ and $0.6^\circ C$,
91 respectively. For winter, the trend from 11 to 6 ka is indistinguishable from zero, while cooling of greater than $\sim 0.3^\circ C$
92 from 6 to 0 ka occurred with $>95\%$ likelihood (Figure 2d).

93 94 **Moist Energy Balance Model**

95 To evaluate how orbitally-driven insolation changes may explain the WAIS Divide reconstructed temperatures (Figure
96 2), we first simulated temperature history at $80^\circ S$ using a global, zonal-mean (2° resolution) moist energy balance

97 model (MEBM) accounting for incoming and outgoing radiation, albedo, and meridional atmospheric heat transport
98 (Methods Section 4). The model is driven by top-of-atmosphere seasonal insolation changes (Figure 3a-e); for this
99 latitude, the maximum summer insolation increases until ~2.5 ka and annual mean and annual- and summer-integrated
100 values mostly decline through the Holocene. The calculations yield summer maximum temperatures and seasonal
101 temperature amplitudes (Figure 3g) that covary with local maximum summer insolation (Figure 3e), and with the
102 general pattern of our reconstructed summer temperatures (ED Figure 7). While heating at lower latitudes can
103 influence Antarctic temperature through atmospheric and oceanic heat transport, modeled maximum summer
104 temperatures at WAIS Divide correlate best with local insolation (70 to 90°S, $R^2 = 0.9$, $p \ll 0.001$ during 0 to 6 ka)
105 rather than insolation anywhere in the subtropical through subpolar latitudes (20 to 60°S, $R^2 = 0.33$ to 0.55 , $p < 0.05$).
106 Indeed, models indicate heat export from WAIS Divide in summer (ED Figure 4k), rather than import from more
107 northern locations. Since December is always the month of maximum insolation (Figure 3a-c), variability of December
108 insolation dominates the response of maximum summer temperature. For winter, modeled temperatures are less
109 variable than those of summer at 80°S (Figure 3g) due to the lack of direct insolation (Figure 3b), and have an opposite
110 trend. Winter minima are a function of three factors: changes in the length of the zero-insolation season, the effective
111 cooling rate of the surface, and convergent heat transport from lower latitudes. Lower minimum winter temperatures
112 occur at times when the zero-insolation season is longer. However, neither the length of the zero-insolation season,
113 modeled minimum temperatures, nor winter heat divergence correlate well with reconstructed winter temperatures.

114 115 **HadCM3 Simulations**

116 To investigate the role of more-complex geography and mechanisms, including topographical changes not accounted
117 for in the MEBM, we simulated Holocene climate with a fully-coupled general circulation model, HadCM3³⁶
118 (Methods Section 5). Simulations forced solely by changes in orbital parameters produce summer maximum
119 temperatures (for approximately the December solstice) at 80°S similar to our reconstructed values and to the MEBM:
120 increasing over the Holocene, peaking at 4 to 3 ka, and decreasing into the modern (ORBIT, Figure 2a). This pattern
121 reflects a strong role of maximum summer insolation in determining observed summer temperatures. The similarity
122 of the early- to mid-Holocene (11-6 ka) summer temperature increase in the orbitally forced HadCM3 simulations and
123 our reconstruction suggests little influence of changing ice-sheet elevation and extent. A similar comparison for winter
124 yields a ~1.25°C decrease of model ORBIT temperature (Figure 2c) compared to a possible small increase in
125 temperature in the reconstruction (Figure 2d; >90% chance of >0.1°C), suggesting some warming due to a lowering
126 ice sheet.

127
128 Next, as boundary conditions in the HadCM3 simulations, we prescribed variable greenhouse gas concentrations and
129 two different ice sheet histories, GLAC1D and ICE-6G, which entail net surface lowerings of ~83 m and ~208 m,
130 respectively, from 11 to 7 ka at the WDC site (Figure 4a). These elevation scenarios substantially affect simulated
131 temperatures (Figure 2a,c). Much of the elevation-induced warming in these models, which occurs primarily in the
132 early Holocene, can be attributed directly to the surface lapse-rate effect (Figure 4b). However, comparison to the
133 orbital-only runs (Figure 4c) reveals a remaining temperature anomaly (Figure 4d), attributable to greenhouse gases,

134 ice sheet extent, and nonlinear responses to simultaneously imposed forcings. Sea ice has only a small impact on the
135 temperature at 80°S in summer (Methods Section 5.4, ED Figure 6).

136
137 Inconsistencies exist between the different ice sheet scenarios (Figure 4d) and the summer vs. winter seasons, but
138 differences are minor enough to permit a bounded estimate of the true Holocene elevation decrease. This calculation
139 is made by comparing the excess of the reconstructed temperature increase over the orbital-only simulation to the
140 same excess for the ice sheet model simulations, and scaling to the elevation changes used in the latter (Methods
141 Section 6). We find central estimates for elevation decrease of 23 m and 53 m from comparison to the GLAC-1D and
142 ICE-6G scenarios, respectively, over the period 10 to 3.5 ka (Table 1). Accounting for uncertainties in the seasonal
143 temperature reconstructions (Figure 2) allows for elevation changes ranging from 33 m increase to 131 m decrease
144 (2σ) from 10 to 3.5 ka, or 54 m increase to 162 m decrease (2σ) if the time interval is narrowed to 10 ka to 6.5 ka
145 (Table 1). Our results thus are consistent with geological observations of ice high-stands on mountain nunataks, which
146 indicate less than 100 m of Holocene surface lowering^{4,5,6}.

147
148 Winter temperatures on the Antarctic mainland must respond to insolation forcings indirectly, via heat transport from
149 lower latitudes. Orbital forcing models predict winter cooling across the Holocene, mostly from 11-6 ka (Figure 2c,
150 3g). Both models and reconstructed winter temperatures lack a late Holocene maximum. But in the earlier Holocene,
151 the winter reconstruction does not display the cooling trend expected from models and is dominated by prominent
152 millennial variations. The mismatch with insolation at lower latitudes and absence of local forcings suggests variations
153 in the efficacy of meridional atmospheric heat transport.

154 155 **Discussion**

156 Diverse and numerous proxies are used to reconstruct globally-averaged surface temperatures for evaluating climate
157 models and distinguishing natural from anthropogenic climate variability^{33,34,41,42,43}. How these proxies depend on
158 seasonal factors has been assessed in only a few cases⁴⁴. Our West Antarctic study provides a cautionary example, as
159 the mean-annual temperature history reflects different controlling factors of summer and winter temperatures whose
160 importance varies with time. In such a situation, important seasonal dynamics may be missed, or proxies
161 misinterpreted, when only mean climate is considered. In addition, incorporating more information from the Southern
162 polar regions should help global temperature assessments avoid biases associated with weighting of temperature
163 reconstructions toward northern sites, which have produced differing interpretations of the relationship between global
164 climate and forcings in the Holocene, even including opposing trends^{34,45,46}.

165
166 Prior analyses with simplified atmospheric models³ identified the duration of Southern Hemisphere summer as a key
167 driving variable of Antarctic climate at orbital timescales. Some paleoclimate findings validate this claim; for example,
168 the onset of deglacial warming in West Antarctica corresponds with increasing integrated summer insolation². Our
169 results – spanning about half a precession-cycle – reveal a dominant role for annual maximum insolation in

170 determining West Antarctic summer climate during the Holocene, without precluding a greater role for duration or
171 integrated summer insolation in other periods, such as glacial terminations.
172

173 **References**
174 1. Berger, A. Milankovitch theory and climate. *Reviews of geophysics*, **26**, 624-657 (1988).
175
176 2. WAIS Divide Project Members. Onset of deglacial warming in West Antarctica driven by local orbital forcing.
177 *Nature*, **500**, 440-444 (2013).
178
179 3. Huybers, P. & Denton, G. Antarctic temperature at orbital timescales controlled by local summer duration. *Nature*
180 *Geoscience*, **1**, 787-792 (2008).
181
182 4. Ackert, R. P., Barclay, D. J., Borns, H. W., Calkin, P. E., Kurz, M. D., Fastook, J. L., & Steig, E. J. Measurements
183 of past ice sheet elevations in interior West Antarctica. *Science*, **286**, 276-280 (1999).
184
185 5. Steig, E. J., Fastook, J. L., Zweck, C., Goodwin, I. D., Licht, K. J., White, J. W., & Ackert Jr, R. P. West
186 Antarctic ice sheet elevation changes. *The West Antarctic Ice Sheet: Behavior and Environment*, **77**, 75-90 (2001).
187
188 6. Ackert, R. P., Mukhopadhyay, S., Parizek, B. R., & Borns, H. W. Ice elevation near the West Antarctic Ice Sheet
189 divide during the last glaciation. *Geophysical Research Letters*, **34**, (2007).
190
191 7. Spector, P., Stone, J., & Goehring, B. Thickness of the divide and flank of the West Antarctic Ice Sheet through
192 the last deglaciation. *The Cryosphere*, **13**, 3061-3075. (2019).
193
194 8. Roe, G. In defense of Milankovitch. *Geophysical Research Letters*, **33**, (2006).
195
196 9. Ganopolski, A., & Brovkin, V. Simulation of climate, ice sheets and CO2 evolution during the last four glacial
197 cycles with an Earth system model of intermediate complexity. *Climate of the Past*, **13**, 1695-1716 (2017).
198
199 10. Buizert, C., Keisling, B. A., Box, J. E., He, F., Carlson, A. E., Sinclair, G., & DeConto, R. M. Greenland-wide
200 seasonal temperatures during the last deglaciation. *Geophysical Research Letters*, **45**, 1905-1914 (2018).
201
202 11. Petit, J. R., Jouzel, J., Raynaud, D., Barkov, N. I., Barnola, J. M., Basile, I., Bender, M., Chappellaz, J., Davis,
203 M., Delaygue, G., Masson-Delmotte, V., Kotlyakov, V.M., Legrand, M., Lipenkov, V. Y., Lorius, C., Pepin,
204 L., Ritz, C., Saltzman, E. & Stievenard, M. Climate and atmospheric history of the past 420,000 years from the
205 Vostok ice core, Antarctica. *Nature*, **399**, 429-436 (1999).
206
207 12. EPICA Community Members. Eight glacial cycles from an Antarctic ice core. *Nature*, **429**, 623-628 (2004).
208
209 13. Bender, M. L. Orbital tuning chronology for the Vostok climate record supported by trapped gas
210 composition. *Earth and Planetary Science Letters*, **204**, 275-289 (2002).

211

212 14. Alley, R. B., & Anandakrishnan, S. Variations in melt-layer frequency in the GISP2 ice core: implications for
 213 Holocene summer temperatures in central Greenland. *Annals of Glaciology*, **21**, 64-70 (1995).

214

215 15. deMenocal, P., Ortiz, J., Guilderson, T., Adkins, J., Sarnthein, M., Baker, L., & Yarusinsky, M. Abrupt onset
 216 and termination of the African Humid Period:: rapid climate responses to gradual insolation forcing. *Quaternary
 217 science reviews*, **19**, 347-361 (2000).

218

219 16. Huybers, P. Antarctica's orbital beat. *Science*, **325**, 1085-1086 (2009).

220

221 17. Laepple, T., Werner, M., & Lohmann, G. Synchronicity of Antarctic temperatures and local solar insolation on
 222 orbital timescales. *Nature*, **471**, 91-94 (2011).

223

224 18. Jones, T. R., Roberts, W. H. G., Steig, E. J., Cuffey, K. M., Markle, B. R., & White, J. W. C. Southern
 225 Hemisphere climate variability forced by Northern Hemisphere ice-sheet topography. *Nature*, **554**, 351-355 (2018).

226

227 19. White, J. W. C. et al. "Stable Isotopes of Ice in the Transition and Glacial Sections of the WAIS Divide Deep Ice
 228 Core" U.S. Antarctic Program (USAP) Data Center. (2019). doi: <https://doi.org/10.15784/601274>.

229

230 20. Jones, T. R. et al. "Mid-Holocene high-resolution water isotope time series for the WAIS Divide ice core". U.S.
 231 Antarctic Program (USAP) Data Center. (2020). doi: <https://doi.org/10.15784/601326>.

232

233 21. Jones, T. R., White, J. W. C., Steig, E. J., Vaughn, B. H., Morris, V., Gkinis, V., Markle, B. R., & Schoenemann,
 234 S. W. Improved methodologies for continuous-flow analysis of stable water isotopes in ice cores, *Atmos. Meas.
 235 Tech.*, **10**, 617–632 (2017a).

236

237 22. Sigl, M., Fudge, T. J., Winstrup, M., Cole-Dai, J., Ferris, D., McConnell, J. R., Taylor, K.C., Welten, K. C.,
 238 Woodruff, T. E., Adolphi, F., Bisiaux, M., Brook, E. J., Buizert, C., Caffee, M. W., Dunbar, N. W., Edwards, R.,
 239 Geng, L., Iverson, N., Koffman, B., Layman, L., Maselli, O. J., McGwire, K., Muscheler, R., Nishiizumi, K.,
 240 Pasteris, D. R., Rhodes, R. H., & Sowers, T.A. The WAIS Divide deep ice core WD2014 chronology–Part 2:
 241 Annual-layer counting (0–31 ka BP). *Climate of the Past*, **12**, 769-786 (2016).

242

243 23. Vinther, B. M., Jones, P. D., Briffa, K. R., Clausen, H. B., Andersen, K. K., Dahl-Jensen, D., & Johnsen, S. J.
 244 Climatic signals in multiple highly resolved stable isotope records from Greenland. *Quaternary Science Reviews*, **29**,
 245 522-538 (2010).

246

247 24. Hughes, A. G., Jones, T. R., Vinther, B. M., Gkinis, V., Stevens, C. M., Morris, V., Vaughn, B. H., Holme, C.,

248 Markle, B. R., & White, J. W. High-frequency climate variability in the Holocene from a coastal-dome ice core in
249 east-central Greenland. *Climate of the Past*, **16**, 1369-1386 (2020).
250

251 25. Morgan, V., & van Ommen, T. D. Seasonality in late-Holocene climate from ice-core records. *The Holocene*, **7**,
252 351-354 (1997).
253

254 26. Jones, T. R., Cuffey, K. M., White, J. W. C., Steig, E. J., Buizert, C., Markle, B. R., McConnell, J. R. & Sigl, M.
255 Water isotope diffusion in the WAIS Divide ice core during the Holocene and last glacial, *J. Geophys. Res. Earth*
256 *Surf.*, **122** (2017b).
257

258 27. Johnsen, S. J., H. B. Clausen, K. M. Cuffey, G. Hoffmann, J. Schwander, & T. Creyts. Diffusion of stable
259 isotopes in polar firm and ice: The isotope effect in firm diffusion, in *Physics of Ice Core Records*, edited by T.
260 Hondoh. pp. 121 – 140, Hokkaido Univ. Press, Sapporo (2000).
261

262 28. Vinther, B. M., Johnsen, S. J., Andersen, K. K., Clausen, H. B., & Hansen, A. W. NAO signal recorded in the
263 stable isotopes of Greenland ice cores, *Geophys. Res. Lett.*, **30**, 1387 (2003).
264

265 29. Markle, B. R. & Steig, E. J. Improving temperature reconstructions from ice-core water-isotope records. *Climate*
266 *of the Past*, **18**, 1321-1368 (2022).
267

268 30. Cuffey, K. M., G. D. Clow, E. J. Steig, C. Buizert, T. J. Fudge, M. Koutnik, E. D. Waddington, R. B. Alley, & J.
269 P. Severinghaus. Deglacial temperature history of West Antarctica, *Proc. Natl. Acad. Sci.*, **113**, 14249-14254
270 (2016).
271

272 31. Steig, E. J., Ding, Q., White, J. W. C., Kuttel, M., Rupper, S. B., Neumann, T. A., Neff, P. D., Gallant, A. J. E.,
273 Mayewski, P. A., Taylor, K. C., Hoffmann, G., Dixon, D. A., Schoenemann, S. W., Markle, B. R., Fudge, T. J.,
274 Schneider, D. P., Schauer, A. J., Teel, R. P., Vaughn, B. H., Burgener, L., Williams, J., & Korotkikh, E. Recent
275 climate and ice-sheet changes in West Antarctica compared with the past 2000 years, *Nat. Geosci.*, **6**, 372–375
276 (2013).
277

278 32. Stenni, B., Curran, M. A., Abram, N. J., Orsi, A., Goursaud, S., Masson-Delmotte, V., Neukom, R., Goosse, H.,
279 Divine, D., van Ommen, T., Steig, E. J., Dixon, D. A., Thomas, E. R., Bertler, N. A. N., Isaksson, E., Ekaykin, A.,
280 Werner, M., & Frezzotti, M. Antarctic climate variability on regional and continental scales over the last 2000
281 years. *Clim. Past.*, **13**, 1609-1634 (2017).
282

283 33. Marcott, S. A., Shakun, J. D., Clark, P. U., & Mix, A. C. A reconstruction of regional and global temperature for
284 the past 11,300 years. *Science*, **339**, 1198-1201 (2013).

- 285
286 34. Kaufman, D., McKay, N., Routson, C., Erb, M., Dätwyler, C., Sommer, P. S., Heiri, O., & Davis, B. Holocene
287 global mean surface temperature, a multi-method reconstruction approach. *Scientific data*, **7**, 1-13 (2020).
288
- 289 35. Huybers, P. Combined obliquity and precession pacing of late Pleistocene deglaciations. *Nature*, **480**, 229-232
290 (2011).
291
- 292 36. Singarayer, J. S., & Valdes, P. J. High-latitude climate sensitivity to ice-sheet forcing over the last 120kyr.
293 *Quaternary Science Reviews*, **29**, 43-55 (2010).
294
- 295 37. Briggs, R. D., Pollard, D., & Tarasov, L. A data-constrained large ensemble analysis of Antarctic evolution since
296 the Eemian. *Quaternary science reviews*, **103**, 91-115 (2014).
297
- 298 38. Argus, D. F., Peltier, W. R., Drummond, R., & Moore, A. W. The Antarctica component of postglacial rebound
299 model ICE-6G_C (VM5a) based on GPS positioning, exposure age dating of ice thicknesses, and relative sea level
300 histories. *Geophysical Journal International*, **198**, 537-563 (2014).
301
- 302 39. Masson-Delmotte, V., Hou, S., Ekaykin, A., Jouzel, J., Aristarain, A., Bernardo, R. T., Bromwich, D., Cattani,
303 O., Delmotte, M., Falourd, S., Frezzotti, M., Gallee, H., Genoni, L., Isaksson, E., Landais, A., Helsen, M. M.,
304 Hoffmann, G., Lopez, J., Morgan, V., Motoyama, H., Noone, D., Oerter, H., Petit, J. R., Royer, A., Uemura, R.,
305 Schmidt, G. A., Schlosser, E., Simoes, J. C., Steig, E. J., Stenni, B., Stievenard, M., van den Broeke, M. R., van de
306 Wal, R. S. W., van de Berg, W. J., Vimeux, F., & White, J. W. C. A review of Antarctic surface snow isotopic
307 composition: observations, atmospheric circulation and isotopic modeling. *J. Climate*, **21**, 3359–3387 (2008).
308
- 309 40. Fortuin, J. P. F. & Oerlemans, J. Parameterization of the annual surface temperature and mass balance of
310 Antarctica. *Annals of Glaciology*, **14**, 78-84 (1990).
311
- 312 41. Shakun, J. D., Clark, P. U., He, F., Marcott, S. A., Mix, A. C., Liu, Z., Otto-Bliesner, B., Schmittner, A., & Bard,
313 E. Global warming preceded by increasing carbon dioxide concentrations during the last deglaciation. *Nature*, **484**,
314 49-54 (2012).
315
- 316 42. Marsicek, J., Shuman, B. N., Bartlein, P. J., Shafer, S. L., & Brewer, S. Reconciling divergent trends and
317 millennial variations in Holocene temperatures. *Nature*, **554**, 92-96 (2018).
318
- 319 43. Osman, M. B., Tierney, J. E., Zhu, J., Tardif, R., Hakim, G. J., King, J., & Poulsen, C. J. Globally resolved
320 surface temperatures since the Last Glacial Maximum. *Nature*, **599**, 239–244 (2021).
321
- 322 44. Bova, S., Rosenthal, Y., Liu, Z., Godad, S. P., & Yan, M. Seasonal origin of the thermal maxima at the Holocene

323 and the last interglacial. *Nature*, **589**, 548-553 (2021).

324

325 45. Liu, Z., Zhu, J., Rosenthal, Y., Zhang, X., Otto-Bliesner, B. L., Timmermann, A., Robin, S. S., Lohmann, G.,
326 Zheng, W., & Timm, O. E. The Holocene temperature conundrum. *Proc. Natl. Acad. Sci.*, **111**, E3501-E3505
327 (2014).

328

329 46. Bader, J., Jungclaus, J., Krivova, N., Lorenz, S., Maycock, A., Raddatz, T., Schmidt, H., Toohey, M., Wu, C., &
330 Claussen, M. Global temperature modes shed light on the Holocene temperature conundrum. *Nature*
331 *communications*, **11**, 1-8 (2020).

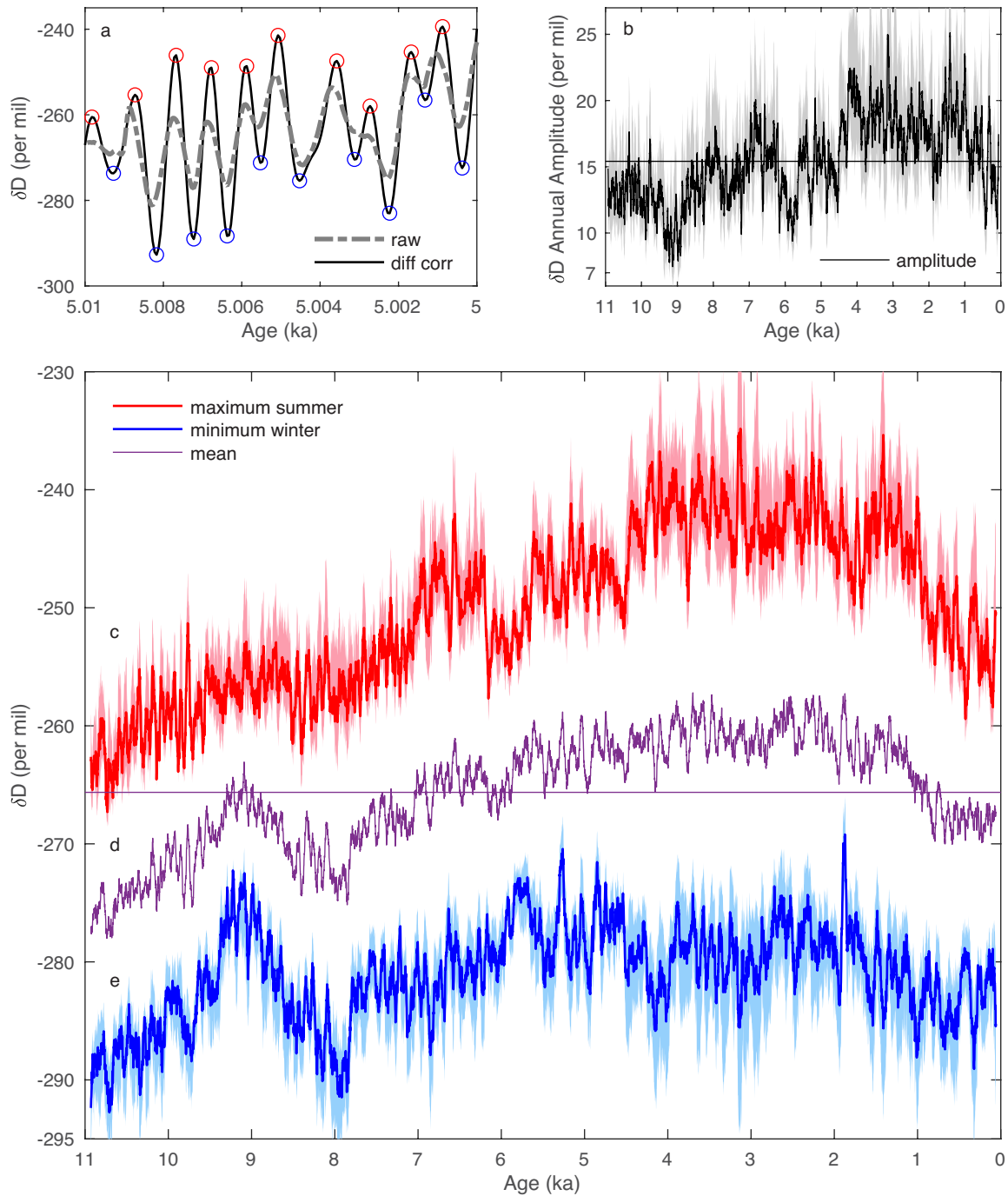
332

333
334
335
336

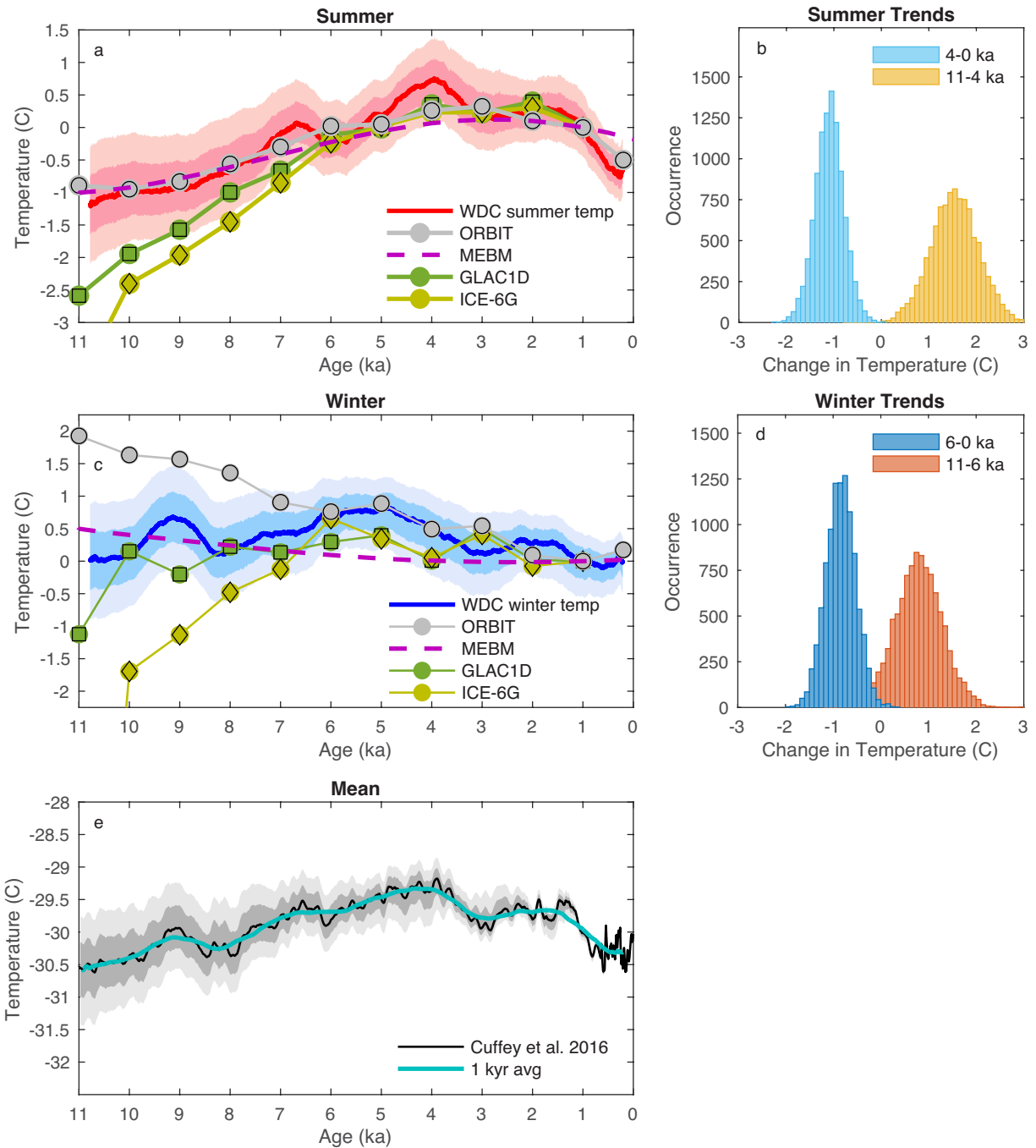
Table 1 | WAIS Elevation Change. *Elevation decrease estimates in meters (2σ , positive values correspond to a lowering ice sheet) for the intervals 10 to 6.5 ka and 10 to 3.5 ka (Methods Section 6).*

Interval	GLAC1D			ICE-6G		
	-2σ	Nominal	2σ	-2σ	Nominal	2σ
10 to 6.5 ka	-9.93	25.67	58.75	-54.00	57.52	161.96
10 to 3.5 ka	-5.63	22.99	48.49	-33.23	52.63	130.53

337
338

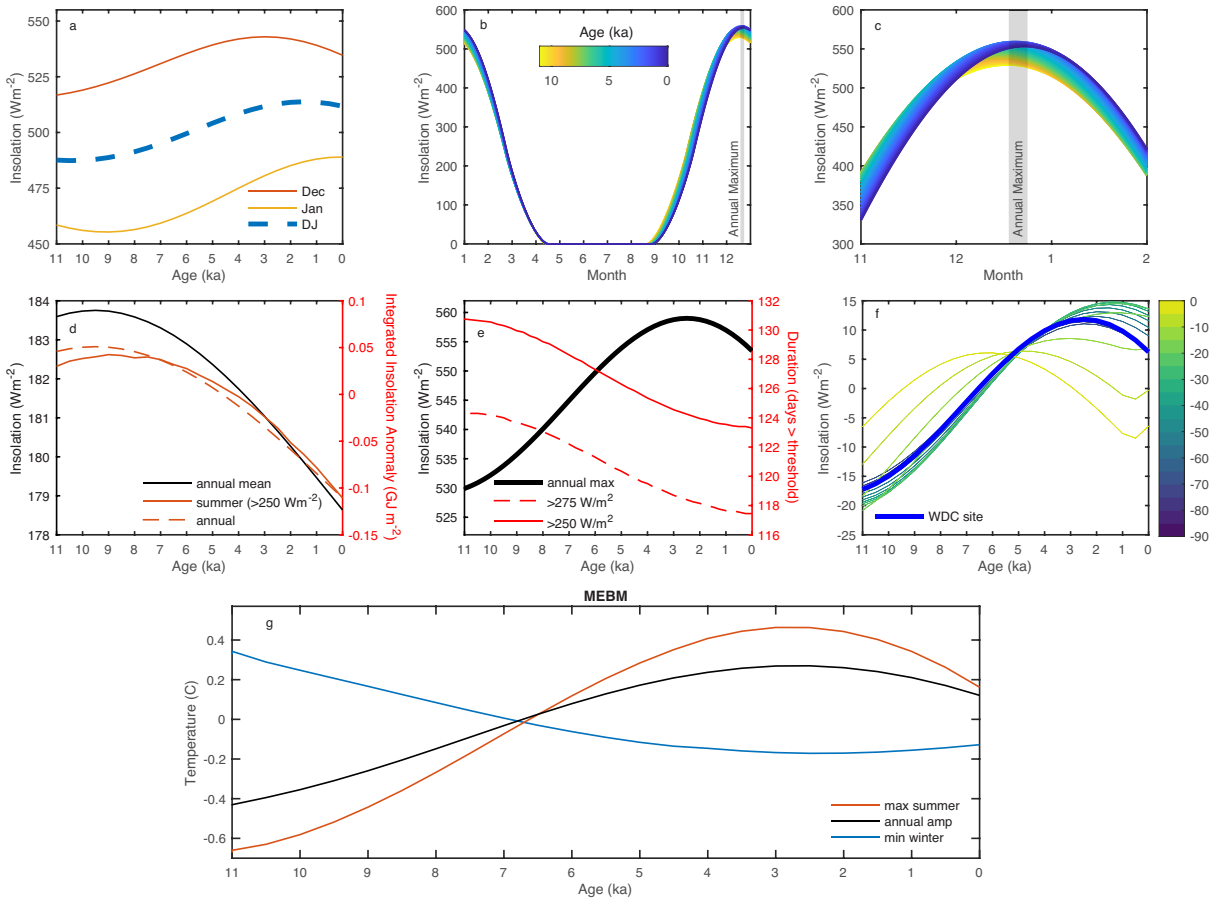


339
 340
 341 **Figure 1 | Water isotope seasonal variability.** *a*, Example section of the diffusion-corrected (solid line) and raw²⁰
 342 (dashed line) WDC δD records, with annual maxima (red circles) and minima (blue circles) determined
 343 algorithmically (Methods Section 2.1). Extended Data (ED) Figure 1 provides the full high-resolution WDC δD
 344 record, diffusion lengths, and extrema. *b*, 50-yr annual-amplitude averages (summer minus winter divided by 2), with
 345 2σ uncertainty; horizontal line indicates Holocene mean. *c*, *d*, *e*, 50-yr δD averages for summer (red), mean (purple),
 346 and winter (blue); horizontal line indicates Holocene mean; shaded regions are 2σ bounds for combined analytical
 347 and diffusion-correction uncertainty.
 348

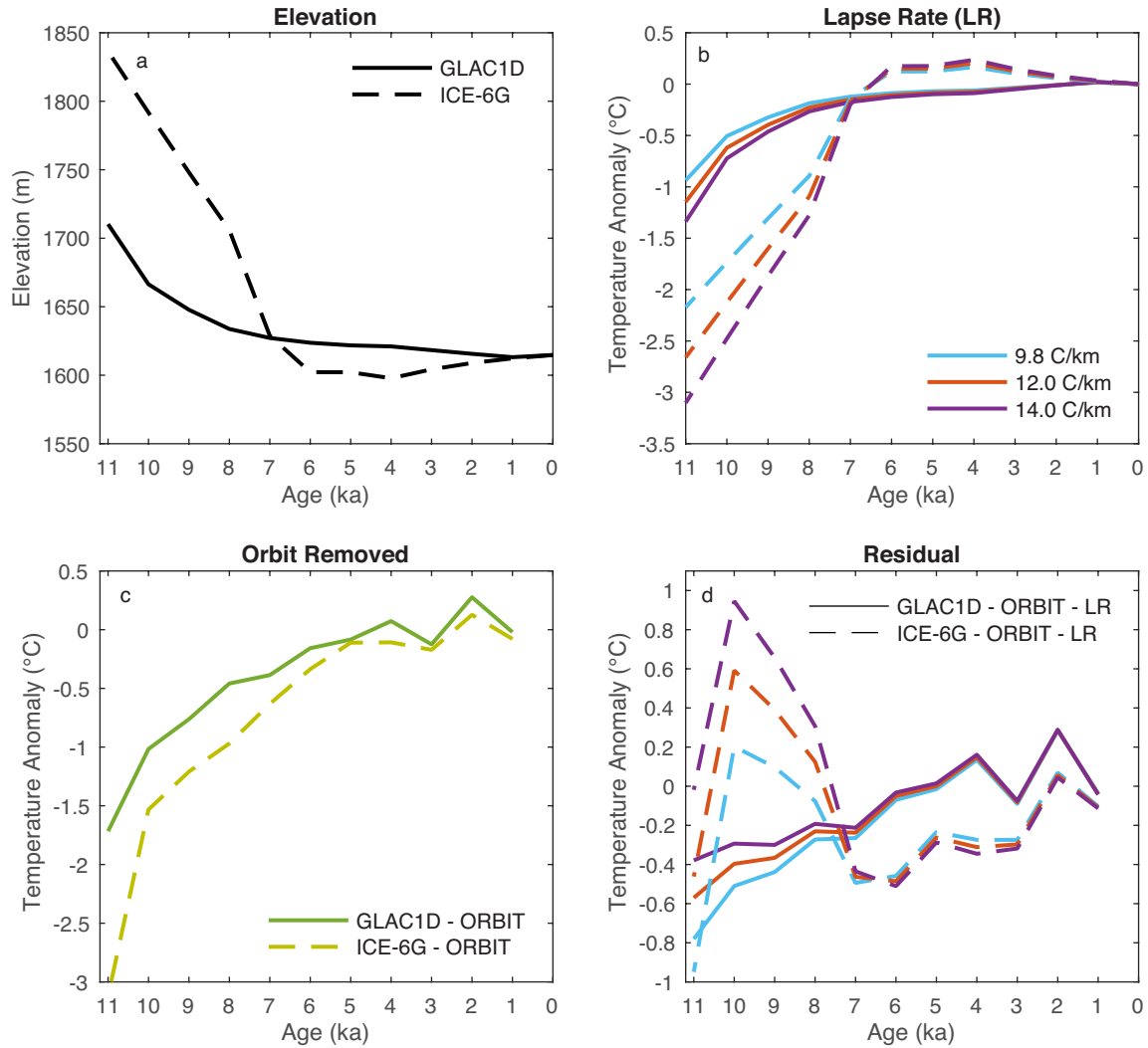


349
 350 **Figure 2 | Seasonal temperature reconstruction.** *a,c*, Reconstructed summer and winter temperatures at WDC for
 351 1,000-year averaging (solid red and blue lines). Shaded regions are 1σ and 2σ uncertainty ranges for combined
 352 uncertainties arising from analysis, diffusion-correction, seasonality of accumulation, precipitation intermittency,
 353 isotope-temperature scaling, and reconstructed mean temperatures (Methods Section 3). Also shown are Moist Energy
 354 Balance Model (MEBM) calculated temperatures for 80°S (maximum and minimum annual values) and HadCM3
 355 zonal temperatures for 80°S (late-December for summer, mid-August for winter) (ORBIT, GLAC1D, ICE-6G). The 0
 356 ka ORBIT simulation uses pre-industrial settings, a calculation not available for GLAC1D or ICE-6G. Normalization
 357 is done at 1 ka when all model runs intersect within 0.05K and the ice sheet configuration is well known. The ICE-6G
 358 values at 11 ka for summer and winter (not shown on plots) are -3.93 K and -10.82 K, respectively. Coefficient of
 359 determinations for model results vs. WDC temperatures (ED Figure 7) are high for summer (HadCM3 ORBIT $R^2 =$

360 0.93, $p \ll 0.001$; *MEBM* $R^2 = 0.80$, $p \ll 0.001$), but not for winter (*HadCM3 ORBIT* $R^2 = 0.00$, $p = 0.85$; *MEBM*
 361 $R^2 = 0.05$, $p = 0.30$). The winter agreement improves if only the period 0 – 6 ka is considered (*HadCM3 ORBIT* $R^2 =$
 362 0.74 , $p = 0.01$; *MEBM* $R^2 = 0.39$, $p = 0.02$). **b,d**, Histograms of net temperature changes over the specified time
 363 intervals, derived by Monte Carlo analysis accounting for systematic and non-systematic uncertainties (*Methods*
 364 *Section 3.5*). **e**, *WDC* mean-annual temperature with 1σ and 2σ uncertainty bounds³⁰. *ED Table 2* shows the amount
 365 of variability in the mean-annual temperature that can be explained by the summer and winter temperatures.
 366
 367



368
 369 **Figure 3 | Temporal and Spatial Variability in Insolation and Model Temperatures.** **a**, Insolation change through
 370 the Holocene³⁵ for December and January, and their average. December best resembles the *WDC* summer
 371 reconstruction. **b**, The full seasonal cycle of insolation at 80°S for 500-yr snapshots over the Holocene. Line colors in
 372 (b) and (c) correspond to age. **c**, Zoom of summer insolation. The maximum always occurs in the latter half of
 373 December (grey shading), migrating across 8 days over the course of the Holocene. **d**, Holocene trends of annual
 374 mean insolation (black), annual integrated insolation (dashed red line), and summer-integrated insolation (red line).
 375 **e**, Maximum summer insolation intensity (black line) and summer duration (red lines), defined as the number of days
 376 above a threshold insolation value each year. **f**, Anomaly in maximum insolation colored by latitude in the Southern
 377 Hemisphere. The thick blue line shows the latitude of the *WDC* site. **g**, Calculated temperatures for 80°S using the
 378 *MEBM*, including maximum summer value (red), minimum winter value (blue), and amplitude of the seasonal
 379 temperature cycle (black).
 380



381
 382
 383 **Figure 4 | Possible ice elevation histories and the corresponding modeled temperatures.** *a*, Elevation histories
 384 used in HadCM3. *GLAC1D*³⁷ is 96 meters higher at 11ka compared to present, and *ICE-6G*³⁸ is 222 meters higher.
 385 *b*, Temperature anomalies from elevation change (*GLAC1D* solid lines; *ICE-6G* dashed lines) using an atmospheric
 386 lapse rate of 9.8°C/km, and spatial lapse rates for interior West Antarctica of 12°C/km³⁹ and 14°C/km⁴⁰. *c*, HadCM3
 387 residual-temperature anomalies for December (summer) calculated by subtracting the ORBIT run from the *GLAC1D*
 388 and *ICE-6G* runs in Figure 2a, highlighting the portion attributable to changing elevation rather than insolation. *d*,
 389 Residual temperature change in (b) subtracted from the results in (c), showing the component driven from processes
 390 besides the direct lapse-rate effect and orbital forcing.

391
 392
 393
 394
 395
 396

397 **Methods**

398 We measured WAIS Divide core (WDC) water isotopes using continuous flow analysis (Section 1), and then corrected
399 for cumulative diffusion using spectral techniques to determine diffusion lengths and restore pre-diffused amplitudes
400 within 140-yr sliding windows (Section 2, ED Figure 1c). Summer maxima and winter minima (Figure 1a) identified
401 in these corrected data were then used to calculate summer and winter amplitudes for each year. We converted the
402 isotope-amplitudes to temperature-amplitudes using a model-determined scaling factor (Section 2.2), and added them
403 to previously reconstructed mean annual temperatures³⁰ to recover summer and winter values. Significant seasonal
404 noise processes required multi-centennial to millennial averaging to reduce uncertainty (Section 3). To elucidate
405 physical controls on sub-annual temperatures, we used a simple energy balance model and HadCM3, a General
406 Circulation Model, to calculate expected changes in seasonal and monthly surface temperatures through time under
407 varying boundary conditions (Sections 4 and 5). Finally, using both observations and modeling, we estimated the
408 change in WAIS surface elevation through the Holocene (Section 6).

409

410 **1 Water Isotopes**

411 WDC water isotopes (ED Figure 1a) were analyzed on a continuous flow analysis system²¹ using a Picarro Inc. cavity
412 ring-down spectroscopy (CRDS) instrument, model L2130-*i*. Using permutation entropy⁴⁷, we identified data
413 anomalies arising from laboratory analysis, which were corrected, including by resampling ice through 1035.4-1368.2
414 m depths (4517-6451 yrs)⁴⁸. All other Holocene data are previously published^{18,31}, and available online^{19,20}. Data are
415 reported in 5-mm increments in delta-notation (per mil, ‰) relative to Vienna Standard Mean Ocean Water (VSMOW,
416 $\delta^{18}\text{O} = \delta\text{D} = 0\text{‰}$), normalized to Standard Light Antarctic Precipitation (SLAP, $\delta^{18}\text{O} = -55.5\text{‰}$, $\delta\text{D} = -428.0\text{‰}$). WDC
417 is annually dated, with accuracy better than 0.5% of the age between 0-12 ka²². For the Holocene, the temporal spacing
418 of consecutive 5 mm samples is < 0.1 years, and the average < 0.05 years, ranging from ~ 2.6 weeks at 10 ka to one-
419 half week from 1-0 ka¹⁸.

420

421 **2 Diffusion Corrections**

422 Diffusion in the firn and deeper ice attenuates high-frequency water-isotope information in ice cores^{26,27,49,50,51,52}.
423 Diffusion length quantifies the statistical vertical displacement of water molecules from their original position^{27,49}. We
424 used diffusion-correction code developed by S. Johnsen, University of Copenhagen^{23,24,27,28}, which uses Maximum
425 Entropy Methods (MEM) to invert an observed power density spectrum. As an input to these inversions, we
426 determined diffusion lengths (ED Figure 1c) for 140-year windows using prior methods^{18,26}. The power density
427 spectrum observed in the ice core record $P(f)$, after diffusion, is $P(f) = P_o(f) \exp[-(2\pi f \sigma_z)^2]$, where $P_o(f)$
428 represents the power spectrum of the undiffused signal (per mil²·m), f is the frequency $\frac{1}{\lambda}$ (1/m), λ the signal wavelength
429 (m), z the depth (m), and σ_z the diffusion length (m). The original, pre-diffusion power-density spectrum (i.e.
430 diffusion-corrected) is calculated as $P_o(f) = P(f) \exp(4\pi^2 f^2 \sigma_a^2)$, for diffusion length σ_a (yr). The $\sigma_a = \frac{\sigma_z}{\lambda_{avg}}$, where
431 λ_{avg} is the mean annual layer thickness (m/yr) at a given depth. The diffusion-corrected spectrum takes the form of a
432 series of complex numbers $X_R + iX_I$ vs. f . From this, the amplitude spectrum A is obtained by $A(f) = \sqrt{X_R^2 + X_I^2}$ and

433 the phase spectrum ϕ is obtained by $\phi(f) = \tan^{-1} \left(\frac{X_I}{X_R} \right)$. The real components of the amplitude and phase spectrums
434 give the diffusion-corrected water isotope signal $\delta_o(t)$ as:

$$435 \quad \delta_o(t) = \sum_{i=1}^N A_i \cos(2\pi f_i t + \phi_i)$$

436 Uncertainties on $\delta_o(t)$ are determined using the uncertainty range for diffusion lengths²⁶ calculated in each 140-year
437 window. Before spectral analysis, the isotope data are linearly interpolated at a uniform time interval of 0.05 yr. Our
438 determination of diffusive attenuation and correction arises from the observed frequency spectra themselves and
439 therefore is entirely independent of firn diffusion and densification models.

440

441 **2.1 Seasonal Water-Isotope Amplitudes**

442 To select extrema (summers and winters) in the diffusion-corrected δD signal (Figure 1a, ED Figure 1b), we used the
443 ‘findpeaks’ matlab function. Figure 1c,d show the resulting time series for summer and winter, averaged with a 50-
444 year boxcar filter for clarity of trends. For every year defined in the WDC age-scale, we calculated the averaged
445 diffusion-corrected δD . The difference between the two extrema and this mean define the summer and winter isotope-
446 amplitudes.

447

448 **2.2 Seasonal Temperatures**

449 A linear scaling converted seasonal isotopic-amplitudes to seasonal temperature-amplitudes, using a sensitivity of
450 isotopes to surface temperatures determined by the “Simple Water Isotope Model” (SWIM)²⁹. Finally, to find summer
451 and winter temperatures we added the individual seasonal temperature-amplitudes to the year’s mean temperature
452 obtained previously³⁰ by calibrating the water-isotope record against borehole temperatures and $\delta^{15}N$ constraints on
453 firn thickness.

454

455 SWIM is based on earlier numerical Rayleigh-type distillation models^{53,54}, which simulate the transport and distillation
456 of moisture down climatological temperature gradients. As moist air is transported towards the poles and cools, the
457 saturated vapor pressure decreases nonlinearly, and moisture above saturation is removed by precipitation. The model
458 keeps track of the isotopic fractionations at each step along this distillation process. In most previous simple models,
459 there is an inconsistency in the calculation of the supersaturation that determines the point of condensation and that
460 drives kinetic isotope fractionation. Modifications to these earlier models, employed in SWIM, ensure consistency in
461 the calculation, which results in a smoother relationship between temperature and the δ -values of precipitation, and
462 better agreement with observed spatial patterns of δD and $\delta^{18}O$. Given input of both δD and $\delta^{18}O$ data, SWIM
463 calculates distributions of source temperatures, the temperature gradients of pseudo-adiabatic pathways, and
464 condensation temperature. We used SWIM to derive sensitivities for surface isotope-temperature scalings using
465 diffusion-corrected WDC data to obtain a surface scaling of 6.96‰ $\delta D/^\circ C$. Using raw data, the surface scaling is
466 7.07‰ $\delta D/^\circ C$. In comparison to other isotope-temperature scalings, Buizert et al.⁵⁵ obtain ~6.56‰ $\delta D/^\circ C$ and Cuffey
467 et al.³⁰ ~7.10‰ $\delta D/^\circ C$ (both converted from $\delta^{18}O$ to δD using a factor of 8).

468

469 **3 Uncertainties in Reconstructing Temperatures**

470 We included uncertainties associated with the following factors: measurement analysis, diffusion correction,
471 seasonality of accumulation, precipitation intermittency, modeled isotope-temperature scaling, and mean-temperature
472 history. The ‘analysis uncertainty’ is 0.55‰ for δD (1σ)²¹. The ‘diffusion-correction uncertainty’ is described by Jones
473 et al.²⁶. The uncertainty of the mean temperature reconstruction, calculated previously³⁰, accounts for the majority of
474 uncertainty in the early-Holocene, but a small fraction in the late-Holocene. Sections 3.1-3.3 explain the other
475 uncertainty terms. Uncertainties for some factors (analysis, diffusion correction) can be treated as independent random
476 variables so that, upon time-averaging, their magnitudes decrease as the inverse of the square root of the number of
477 values. Uncertainties for other factors (intermittency, isotope-temperature scaling, mean temperature, seasonality)
478 might be systematically biased, and therefore their magnitudes are taken to be invariant with respect to the interval of
479 averaging. Based upon the 2σ uncertainties for summer and winter temperature (Figure 2a,c), we assessed the
480 significance of dominant trends using Monte Carlo analysis (Figure 2b,d; Section 3.5).

481

482 **3.1 Seasonal Preservation Bias Uncertainty**

483 Unequal seasonal distribution of snowfall could result in different magnitudes of diffusion for winter and summer
484 amplitudes⁴⁹. The seasonal temperature cycle also impacts the magnitude of diffusion for all seasons. We utilized the
485 Community Firn Model (CFM)^{56,57}, a firn-evolution model with coupled firn temperature, firn densification, and
486 water-isotope modules, to test how seasonally weighted accumulation affects the diffusion of specified, hypothetical
487 isotope records progressing from surface snow (δD_{snow}), to consolidated snowpack in the firn (δD_{firn}), to solid ice
488 beneath the pore close-off depth (δD_{ice}). We applied the back-diffusion calculation (Section 2) to δD_{ice} to estimate the
489 original δD_{snow} . We then assessed how reconstructions of δD_{snow} could be misinterpreted due to different seasonal-
490 accumulation weightings (ED Figure 2a,b).

491

492 We performed five CFM runs using monthly time-steps for accumulation, temperature, and isotopes (ED Table 1).
493 The seasonal cycle for δD_{snow} is based on the mean amplitude in Figure 1b (15.43‰). Five WAIS accumulation
494 scenarios were tested based on monthly accumulation from the regional climate model MAR3.6 (Modèle
495 Atmosphérique Régional; ERA-Interim forced)⁵⁸, which spans the period January 1979 to December 2017. The mean
496 accumulation over the entire 39-year period is 0.24745 m ice eq. a^{-1} , with about 1.6x as much snow in winter (Oct-
497 Mar) as summer (Apr-Sep). The five scenarios are as follows. 1) ‘constant’: identical accumulation for all months
498 (0.0206 m ice eq. $month^{-1}$; 1/12 the annual mean). 2) ‘cycle’: monthly accumulation equal to MAR monthly means.
499 3) ‘noise’: using the ‘cycle’ time series, we add noise to each time step in the ‘cycle’ series, we added a normal random
500 variable of zero mean and the standard deviation for the month from MAR, 4) ‘random’: for each month, the
501 accumulation is a normal random variable with mean and standard deviation equal to MAR monthly values. 5) ‘loop’:
502 the entire 39-year MAR accumulation time series is repeated over and over again. For the temperature boundary
503 condition, we used each month’s mean 1979-2017 2m temperature predicted by MAR to create an annual temperature
504 cycle. We repeated this 12-month time series for the duration of the model runs. This method ensures that model runs,

505 which are designed to test accumulation seasonality, are not affected by interannual temperature variability, while also
506 providing an estimate of the annual-temperature cycle, which affects the rate of isotope diffusion in the upper firn.

507
508 ED Figure 2a,b shows the results for the ‘constant’ and ‘cycle’ cases. The diffusion-correction technique accurately
509 reconstructs δD_{snow} for summer and winter in the ‘constant’ snowfall scenario, but underestimates summer values in
510 the MAR ‘cycle’ scenario by $\sim 2.6\text{‰}$, which is 11% of the full range of the observed WDC summer water-isotope
511 values. Winter values are overestimated by only $\sim 0.6\text{‰}$, about 3% of the full winter range, since winter has 1.6x as
512 much snow as summer. The ‘noise’, ‘random’, and ‘loop’ runs produce results within 0.3‰. These CFM experiments
513 demonstrate that centennial trends in the summer and winter water isotopes on the order of a few per mil could arise
514 from large changes in seasonal-accumulation weighting, while multi-millennial trends $\gg 2.6\text{‰}$ are unlikely to be
515 caused by seasonal accumulation and can therefore be interpreted as climate signals of a different origin. For 1,000-
516 year averaging (as in Figure 2), HadCM3 indicates seasonal accumulation weighting (winter:summer) of 1.3 to 1.7
517 throughout the Holocene (ED Figure 2f), which yields a 1σ uncertainty of 0.27‰ based on the CFM testing criteria.

518
519 To determine observationally if seasonal snowfall changed significantly across the Holocene, we used measured black
520 carbon (BC) concentrations, the only age-scale-independent impurity. BC data are available from 0-2.5 ka and 6-11
521 ka. Seasonal-fire regimes in South America dominate BC concentrations at WDC, causing BC maxima and minima
522 in fall and spring, respectively⁵⁹ (ED Figure 2c). We split each year into two parts, characterized by rising or falling
523 BC. Call BC_1 and BC_2 the depth intervals of rising and falling BC. The duration of BC_2 is longer than BC_1 due to
524 source characteristics⁵⁷ (ED Figure 2c), thus $BC_1/BC_2 < 1$ (ED Figure 2e). The BC_1/BC_2 ratio can change with time
525 due to variability at the source, changes in atmospheric transport, or seasonality of snow deposition. We observe little
526 change in BC_1/BC_2 resembling the multi-millennial trends seen in WDC summers and winters (ED Figure 2d,e).
527 Unless there are competing and exactly compensating effects in seasonality (i.e. the source change exactly cancels the
528 depositional and transport change, or other unlikely scenarios), the BC data provide evidence that changes in WDC
529 seasonal snowfall were not large enough to affect our multi-millennial climate interpretations.

530 531 **3.2 Intermittency of Precipitation Uncertainty**

532 The episodic nature of snowfall creates an incomplete record of local climate variations⁶¹, preventing interpretation
533 of trends over short time intervals. We want to interpret isotopic variations averaged over a sufficiently long timescale
534 that, to within a specified tolerance, trends are not likely to be random noise arising from the spread of distributions
535 preserved in the ice. Using distributions of reconstructed annual amplitudes (Figure 1b, ED Figure 2g) for 1,000-year
536 windows throughout the Holocene, we conducted Monte Carlo resampling simulations to determine that 250-year
537 averaging-lengths are needed to achieve a standard error of 1‰, corresponding to a mean amplitude-to-noise ratio of
538 15. For the time period with greatest variability, centered on 4 ka, the standard error for a 1,000-year average (as used
539 in Figure 2) is 0.52‰ (ED Figure 2h). Since this is an amplitude uncertainty (rather than uncertainty associated with
540 a season), we specify the 1σ uncertainties for summer and winter as half of 0.52‰.

541

542 **3.3 Isotope-Temperature Scaling and Associated Uncertainty**

543 The conversion of isotopic values (1,000-year averages) to temperature yields three curves for summer and three for
544 winter: T_{nominal} , $T_{+1\sigma}$, $T_{-1\sigma}$. Each curve is normalized to the value at 1 ka (as done in Figure 2). The difference in
545 the $T_{+1\sigma}$ and $T_{-1\sigma}$ curves gives the 1σ uncertainty range $+\sigma_{T\text{scale}}$ to $-\sigma_{T\text{scale}}$, which are then added in quadrature to
546 the Cuffey et al.³⁰ mean-temperature uncertainties, yielding the final uncertainty estimates shown in Figure 2.

547
548 **3.4 Relationship Between the Annual Mean and Individual Seasons**

549 Using 1,000-year and 300-year averages of summer, winter, and mean temperature (ED Figure 3c-f), we determined
550 R^2 values for summer and winter vs. the mean. We then subtracted the 1,000-year averages from the 300-year averages
551 to obtain residuals, and then determined R^2 values again for summer and winter vs. the mean (ED Table 2). From 11-
552 0 ka, the high summer correlations for the 1,000-year comparison indicate a strong association of the annual-mean
553 temperature with the summer temperature at orbital timescales. At suborbital scales (i.e. the 300 to 1,000-year
554 residuals), neither the summer nor the winter alone explains much of the mean-annual variability, and the annual mean
555 is a random composite of the two seasons. If only 11-7 ka is considered, winter variability explains more of the mean
556 at sub-millennial scales.

557
558 **3.5 Trend Analysis**

559 To assess the significance of dominant trends in our reconstructed seasonal temperatures, we conducted a Monte Carlo
560 analysis founded on the assumption that all possibilities for the unknown time-dependence of errors are equally likely.
561 The essential motivation for this approach is that we have determined the magnitudes of uncertainties as a function of
562 age but that we have no information about whether the errors in our reconstruction persist at similar values for long
563 periods of time (i.e., exhibit a bias) or whether they fluctuate at high-frequency.

564
565 We randomly generated a large number of alternative seasonal temperature histories governed by the uncertainties on
566 1000-year averages (ED Figure 3a,b), calculated the temperature trends for each alternate history over desired time
567 intervals (such as 11-4 ka and 4-0 ka), and compiled the results into frequency distributions from which probabilities
568 can be calculated (Figure 2b,d). Specifically, each alternative history deviates from the summer and winter temperature
569 reconstruction by an amount that smoothly varies over time between random nodes whose values are a Gaussian
570 random variable of zero mean and standard deviation for 1000-year averages at the age of the node. The number of
571 nodes and the age of each node are random variables, uniformly distributed between 1 and 11 nodes and 0-11 ka,
572 respectively. A small number of nodes produce an alternative temperature history for which the bias is serially
573 correlated for millennia, while a large number of nodes produce a history for which the bias is uncorrelated from
574 millennium to millennium.

575
576 **4 Seasonal Moist Energy Balance (MEBM) Model**

577 We used a simple global, zonal-mean moist energy balance model to calculate surface temperatures (ED Figure 4),
578 accounting for top-of-atmosphere (TOA) insolation, temperature-dependent long-wave emission to space,

579 temperature-dependent albedo to simulate brightening by snow and ice, and horizontal atmospheric-heat transport
580 treated as diffusion of near-surface moist static energy^{62,63,64}. The model has a 2-degree spatial resolution, a single
581 surface and single atmospheric layer, and a surface-heat capacity based on the relative fraction of land and ocean
582 surface in the zonal mean. Heat exchange between the surface and atmosphere layers arises from differences in
583 blackbody radiation from each layer, and sensible and latent heat exchanges proportional to temperature and specific
584 humidity contrasts (assuming a constant relative humidity of 80%), following bulk aerodynamic formulae. We
585 calculated the annual TOA insolation-cycle at every latitude in 500-year time slices from 0-11 ka. For each time slice
586 the model is run at 2-hour time resolution for 30 model-years to reach equilibrium.

587
588 ED Figure 4 compares the temporal evolution of annual mean and peak summer heat divergence by the atmosphere
589 ($\nabla \cdot \mathbf{F}$) at the WDC site to the annual mean and summer maximum site temperature and insolation. While Holocene
590 changes in $\nabla \cdot \mathbf{F}$ at the WDC site correlate with insolation forcing, the magnitude of changes in maximum direct
591 insolation are much larger than those in atmospheric heat divergence. Further the Holocene changes in summertime
592 heat divergence are of the wrong sign to cause net heating at the WDC site (positive divergence is an export of heat
593 by the atmosphere from the site). Heat transport in the Antarctic is convergent in the annual mean, but divergent in
594 mid-summer, as intense incoming insolation exceeds longwave emissions from the cold surface.

595

596 **5 HadCM3 model simulations**

597 **5.1 Model setup**

598 We used the fully coupled ocean-atmosphere model HadCM3^{65,66}, version HadCM3BM2.1, which well simulates
599 tropical Pacific climate and its response to glacial forcing⁶⁷. Our simulations are snapshots at 1-kyr intervals over the
600 last 11 ka³⁶, with time-specific boundary conditions of orbital forcing⁶⁸, greenhouse gas (GHG) concentration^{69,70}, ice
601 sheet topography, and sea level^{37,38,71,72,73,74,75}. We used three simulations: 1) only orbital forcing changes (ORBIT),
602 with all other boundary conditions set to the pre-industrial; 2) orbital/GHG forcing with GLAC1D ice-sheet elevation
603 history; and 3) orbital/GHG forcing with ICE-6G ice-sheet elevation history. Elevation histories are shown in Figure
604 4a. Snapshot simulations were run for at least 500 years with analysis made on the final 100 years. Additional snapshot
605 simulations for 10 ka allowed us to decompose the role of different forcings, described in the following sections. The
606 large difference in forcings between 10 ka and the pre-industrial late Holocene make this comparison most instructive.

607

608 **5.2 Summer Climate**

609 We examined the zonal mean at 80°S in simulations for hypothetical 10 ka worlds, by changing the boundary
610 conditions to compare to the pre-industrial/late-Holocene. These simulations are ‘10ka ORBIT-only’; two runs with
611 only ice sheets at 10 ka and pre-industrial settings otherwise, called ‘10 ka GLAC1D-only’ and ‘10ka ICE-6G-only’;
612 and two runs with all 10 ka forcings, called ‘10ka GLAC1D-all’, and ‘10ka ICE- 6G-all’. In ‘10ka ORBIT-only’,
613 reduced TOA shortwave radiation causes a large reduction in shortwave radiation at the surface (SW_d), and consequent
614 cooling. Downward longwave radiation (LW_d) also decreases, likely due to atmospheric cooling. Sensible heat flux
615 (SH_d) to the surface is increased indicating that the atmosphere and surface do not equally cool; one cause of this is
616 the increased meridional heat convergence ($-\nabla \cdot \mathbf{F}$).

617
618 Changed ice sheets cause summertime cooling in both ‘10 ka GLAC1D-only’ and ‘10ka ICE-6G-only’, primarily via
619 reduced LW_d . Increased SW_d , due to reduction of depth of the atmospheric column above the ice sheet surface,
620 counteracts the reduced LW_d to some extent. (Reducing the atmospheric column reduces SW absorption and tends to
621 cool the atmosphere, reducing LW_d). Both ice sheet scenarios also cause an increase in $-\nabla \cdot \mathbf{F}$, partly counteracting
622 summertime cooling.

623
624 Using all 10 ka forcings causes cooling through both LW_d and SW_d . The decrease in SW_d is similar in ‘10ka GLAC1D-
625 all’ and ‘10ka ICE-6G-all’ and slightly smaller than in ‘10ka ORBIT-only’, likely because the thinner atmospheric
626 column reduces absorption. The decrease in LW_d in ‘10ka GLAC1D-all’ and ‘10ka ICE-6G-all’ is larger than in ‘10ka
627 ORBIT-only’, ‘10 ka GLAC1D-only’, and ‘10ka ICE-6G-only’. This indicates the importance of feedbacks in the
628 atmosphere. Heat convergence $-\nabla \cdot \mathbf{F}$ increases in both simulations indicating remote feedbacks, in addition to local
629 feedbacks related to the amount of water vapor in the atmosphere.

630
631 The preceding description of changes in the zonal mean in the 10 ka simulations compared to pre-industrial holds for
632 the entire Holocene. Orbital forcing alone reduces SW_d and LW_d by roughly the same magnitude. With full forcing
633 (including ice sheets), the reduction in LW_d is roughly three times the reduction in SW_d . Considering an energy budget
634 over the WDC site (79.467°S 112.085°W), mechanisms are the same as for the zonal mean. Magnitudes of forcings
635 change, but reduced SW_d still cools the surface, amplified by a LW_d feedback dependent on ice sheet size.

636 637 **5.3 Winter Climate**

638 During winter SW_d is no longer a factor as the sun is below the horizon, yet there is still surface warming caused by
639 an increase in LW_d . An increase in $-\nabla \cdot \mathbf{F}$ in ‘10ka ORBIT-only’ warms the atmospheric temperature, increasing LW_d
640 and SH_d . With an ice sheet imposed the surface temperature cools. In both ‘10 ka GLAC1D-only’ and ‘10 ka ICE-6G-
641 only’ there is a reduction in $-\nabla \cdot \mathbf{F}$, reducing LW_d and SH_d . When all 10 ka forcings are introduced, the change in
642 temperature is smaller than for ice sheet-only runs. In ‘10ka GLAC1D-all’ we found no change in $-\nabla \cdot \mathbf{F}$, LW_d , or
643 surface temperature. This suggests that the increase in $-\nabla \cdot \mathbf{F}$ from orbital forcing is almost perfectly balanced by the
644 change in $-\nabla \cdot \mathbf{F}$ from the ice sheet configuration.

645
646 The processes controlling heat transport over Antarctica are complicated and HadCM3 may not be able to simulate
647 them perfectly. Our simulations indicated that remote processes during winter alter the heat transport, affecting
648 atmospheric and surface temperatures. Raising the topography of Antarctica tends to reduce such heat transport (ED
649 Figure 5), producing an additional cooling on top of a pure lapse rate effect⁷⁶. This cannot, however, explain the
650 prominent millennial-scale changes at ~9.2 and ~7.9 ka (Figure 1e,2c). The intricacies of interpreting the early
651 Holocene winter variability in West Antarctica necessitates further study.

652 653 **5.4 Sea Ice**

654 Sea ice changes may alter local energy fluxes from the ocean to the atmosphere. In HadCM3, sea-ice extent changes
655 across the Holocene. We used two analyses (ED Figure 6) to show sea ice is not a primary control on the surface
656 temperature at WDC (80°S): 1) Correlation analysis of sea-ice changes and surface temperature, and 2) Atmosphere-
657 only model simulations in which we specified individual changes in the model boundary conditions (including sea
658 ice).

659
660 We computed the dominant spatial patterns of sea-ice variability using EOFs across all of the HadCM3 simulations
661 (ALL), and individually for three sub-set simulations (ORBIT, GLAC1D, ICE-6G), from 0-11 ka. We projected the
662 model-simulated sea ice for each individual time-slice simulation onto these patterns to compute the amplitude of sea-
663 ice variability in each simulation. The amplitude was compared to temperature at 80°S to understand how large-scale
664 changes in the sea ice affect temperature for the months of December (summer) and July (winter) (ED Figure 6).

665
666 In winter, we found negligible correlations between sea-ice change and temperature in all sets of simulations (ALL:
667 0.02, ORBIT: 0.04; GLAC1D: 0.16; ICE-6G: 0.06). This suggests that winter sea ice is not an important factor in
668 determining the temperature at 80°S. In summer, only the ORBIT simulation has meaningful correlations between
669 temperature and sea ice variability (ALL: 0.59, ORBIT: 0.84, GLAC1D: -0.60; ICE-6G: 0.36). The sign of the
670 correlation changes between simulations despite the sea-ice change pattern being the same in all simulations. From
671 this we concluded that sea ice is not a dominant control on temperature at 80°S in summer. The correlation in the
672 ORBIT simulations suggests that there may be some relationship between sea ice and temperature; we investigated
673 this with atmosphere-only simulations.

674
675 In atmosphere-only simulations at 0 ka and 10 ka, we specified the top of the atmosphere insolation, SST, and sea ice
676 from the ORBIT simulations. Over land areas and sea-ice regions, the model calculates the surface temperature using
677 the land-surface scheme in the model. The atmosphere model is identical to the model used within the coupled-model.
678 We ran a series of experiments varying the orbital configuration, SST, or sea ice (summarized in ED Table 3).

679
680 The zonal mean of the change in the sea ice that we prescribed can be seen in ED Figure 6e, and the change in the
681 SST can be inferred from ED Figure 6f-h. ED Figure 6f shows that the atmosphere-only model replicates the change
682 in temperature of the coupled-model. ED Figure 6g shows that the effect of the 10 ka orbital configuration
683 ('Atmos_10k_insol') is to cool Antarctica considerably by about 0.5°C. North of 65°S there is no change in the surface
684 temperature, primarily a response to the imposed SST and sea ice, which are the same in the 'Control' and
685 'Atmos_10k_insol'. Imposing the SST and sea ice from 10 ka ('Atmos_10k_ice_SST'), we find very little change in
686 the surface temperature over Antarctica, but there are some large changes in the surface temperature north of 70°S.
687 ED Figure 6h shows the result of imposing 10 ka SST or 10 ka sea ice. The 10 ka SST ('Atmos_10k_SST') tends to
688 warm Antarctica, consistent with the large increases in SST north of 65°S. Changing sea ice ('Atmos_10k_ice') tends
689 to cool Antarctica. Both effects are small, approximately 0.1°C, and of opposite sign. This explains the small net
690 change in the surface-temperature change over Antarctica when SST and sea ice are changed simultaneously, as shown
691 by 'Atmos_10k_SST_ice'. It should be noted that in the coupled system a change in sea ice can not be decoupled from

692 a change in the SST, so not only is the effect of sea ice on the climate small, it is also likely associated with a
693 compensating change in SST. From these simulations we concluded that sea ice and SST changes are not a dominant
694 driver of the change in the surface temperature over Antarctica.

695
696 ED Figure 6e shows that the change in sea ice at 10 ka in ORBIT is much larger than the change in either GLAC1D
697 or ICE-6G. The ORBIT simulations do not account for all of the changes in the boundary conditions at 10 ka and are
698 therefore less realistic than either ICE-6G or GLAC1D. Since ICE-6G and GLAC1D both show much smaller changes
699 in the sea ice and SST than ORBIT, we expect that in reality there is also a much smaller change in the sea ice and
700 SST than in ORBIT. We thus concluded that sea ice has a small impact on the temperature at 80°S in summer.

701
702 We also performed a similar analysis of the winter season (not shown). We found the atmosphere-only model does
703 not compare well with the coupled model, simulating very little change in the surface temperature. Doing a term-by-
704 term decomposition of the atmosphere model is not, therefore, particularly useful as it tells us more about the model
705 rather than the physical climate. The failure of the atmosphere-only model to capture the changes at 10 ka suggests
706 that the importance of the SST and sea ice is in their day-to-day coupling with the atmosphere and not in any long-
707 term mean change in this season.

708

709 **6 Estimating elevation changes**

710 Temperatures simulated by HadCM3 for ORBIT provide a control scenario against which observations can be
711 compared to identify the signal of elevation change. For a chosen time interval, the net reconstructed warming ΔT_R
712 exceeds that of ORBIT by an amount $\Delta T_R - \Delta T_O$. This can be compared to the effective lapse-rate $(\Delta T_M - \Delta T_O) / \Delta Z_M$
713 defined by a HadCM3 simulation including topographic change (GLAC1D or ICE6G models) and all forcings, for
714 model warming ΔT_M and model elevation decrease ΔZ_M . Specifically, the estimated elevation decrease is $\Delta Z_R = \Delta Z_M$
715 $[(\Delta T_R - \Delta T_O) / (\Delta T_M - \Delta T_O)]$. Summer and winter reconstructions offer two separate assessments, for which we
716 calculate the algebraic average.

717

718 Accounting for uncertainties in ΔT_R requires recognizing that uncertainties of summer and winter reconstructions are
719 not independent, while also recognizing that they emerge from two independent sources: uncertainty in the mean
720 annual temperature history (calculated in Cuffey et al.³⁰) and uncertainty in the seasonal amplitude (calculated in the
721 present study). In general, the uncertainty of seasonal temperature at a specified time is the quadrature sum of annual
722 and amplitude uncertainties, which gives 1σ and 2σ uncertainties for a given season and time. However, if the true
723 value of annual temperature is shifted by an amount $\alpha\sigma$ from the nominal reconstruction, this must be true for both
724 summer and winter. And if the true value of amplitude is shifted by an amount $\beta\sigma$ from the nominal reconstruction,
725 the temperature shift must be $+\beta\sigma$ in one season but $-\beta\sigma$ in the other.

726

727 To define bounding cases on elevation change in a specified time interval, we calculated the maximal (or minimal)
728 temperature change ΔT_R for a season by differencing the upper (or lower) limit at one end of the interval with the

729 lower (or upper) limit at the other end, and also calculating the corresponding ΔT_R for the opposite season required by
730 the correlated errors. The elevation decreases ΔZ_R were then calculated by comparison to HadCM3 simulations, as
731 specified previously, and the summer and winter values averaged. This process was completed four times for each
732 time interval and HadCM3 model, corresponding to four different initial ΔT_R (maximum and minimum ΔT_R for
733 summer, and maximum and minimum ΔT_R for winter), and the most extreme case taken as the result (this proved to
734 be the one starting with maximum summer ΔT_R). Table 1 lists results for two time intervals and the two HadCM3
735 simulations with variable topography.

736

737 **Data Availability**

738 The WDC water isotope datasets analyzed during the current study are available in the U.S. Antarctic Program Data
739 Center (USAP-DC) repository, <https://doi.org/10.15784/601274> and <https://doi.org/10.15784/601326>. The impurity
740 datasets analyzed during the current study are available in USAP-DC repository, <https://doi.org/10.15784/601008>.

741
742 The data generated in this study is available in the USAP-DC repository, <https://doi.org/10.15784/601603>, including
743 raw and diffusion-corrected water isotopes, seasonal water isotopes (maximum summer and minimum winter
744 values), and seasonal temperature reconstructions. Additional data are available in the online source files linked to
745 this publication.

746 .

747 **Code Availability**

748 The MATLAB code used for the diffusion correction of water isotope data and the subsequent selection of seasonal
749 extrema (summer and winter) is available online at Zenodo, <https://doi.org/10.5281/zenodo.7042035>.

750

751 **References**

- 752 47. Bandt, C. & Pompe, B. Permutation entropy: a natural complexity measure for time series. *Physical review letters*,
753 **88**, 174102 (2002).
754
- 755 48. Garland, J., Jones, T. R., Neuder, M., Morris, V., White, J. W., & Bradley, E. Anomaly detection in paleoclimate
756 records using permutation entropy. *Entropy*, **20**, 931 (2018).
757
- 758 49. Johnsen, S. J. Stable isotope homogenization of polar firn and ice, Proceedings of Symposium on Isotopes and
759 Impurities in Snow and Ice, *IAHS-AISH Publ.*, **118**, 210–219 (1977a).
760
- 761 50. Whillans, I. M. & Grootes, P. M. Isotopic diffusion in cold snow and firn. *Journal of Geophysical Research*, **90**,
762 3910–3918 (1985).
763
- 764 51. Cuffey, K. M. & Steig, E. J. Isotopic diffusion in polar firn: implications for interpretation of seasonal climate
765 parameters in ice-core records, with emphasis on central Greenland. *Journal of Glaciology*, **44**, 273-284 (1998).
766
- 767 52. Gkinis, V., Simonsen, S. B., Buchardt, S. L., White, J. W. C. & Vinther, B. M. Water isotope diffusion rates from
768 the NorthGRIP ice core for the last 16,000 years – glaciological and paleoclimatic implications. *Earth and Planetary*
769 *Science Letters*, **405**, 132–141 (2014).
770
- 771 53. Ciais, P., & Jouzel, J. Deuterium and oxygen 18 in precipitation: Isotopic model, including mixed cloud
772 processes. *Journal of Geophysical Research: Atmospheres*, **99**, 16793-16803 (1994).
773
- 774 54. Kavanaugh, J. L., & Cuffey, K. M. Space and time variation of $\delta^{18}\text{O}$ and δD in Antarctic precipitation
775 revisited. *Global Biogeochemical Cycles*, **17**, (2003).
776
- 777 55. Buizert, C., Fudge, T. J., Roberts, W. H. G., Steig, E. J., Sherriff-Tadano, S., Ritz, C., Lefebvre, E., Edwards, J.,
778 Kawamura, K., Oyabu, I., Motoyama, H., Kahle, E. C., Jones, T. R., Abe-Ouchi, A., Obase, T., Martin, C., Corr, H.,
779 Severinghaus, J. P., Beaudette, R., Epifanio, J. A., 600 Brook, E. J., Martin, K., Chappellaz, J., Aoki, S., Nakazawa,
780 T., Sowers, T. A., Alley, R. B., Ahn, J., Sigl, M., Severi, M., Dunbar, N. W., Svensson, A., Fegyveresi, J. M., He, C.,
781 Liu, Z., Zhu, J., Otto-Bliesner, B. L., Lipenkov, V. Y., Kageyama, M., & Schwander, J. Antarctic surface temperature
782 and elevation during the Last Glacial Maximum, *Science*, **372**, 1097–1101 (2021).
783
- 784 56. Stevens, C. M., Verjans, V., Lundin, J., Kahle, E. C., Horlings, A. N., Horlings, B. I., & Waddington, E. D. The
785 Community Firn Model (CFM) v1. 0. *Geoscientific Model Development*, **13**, 4355-4377 (2020).
786
- 787 57. Gkinis, V., Holme, C., Kahle, E. C., Stevens, M. C., Steig, E. J., & Vinther, B. M. Numerical experiments on firn
788 isotope diffusion with the Community Firn Model. *Journal of Glaciology*, **67**, 450-472 (2021)..
789

- 790 58. Agosta, C., Amory, C., Kittel, C., Orsi, A., Favier, V., Gallée, H., van den Broeke, M. R., Lenaerts, J. T. M., van
791 Wessems, J. M., van de Berg, W. J., & Fettweis, X. Estimation of the Antarctic surface mass balance using the regional
792 climate model MAR (1979–2015) and identification of dominant processes, *The Cryosphere*, **13**, 281–296 (2019).
793
- 794 59. Arienzo, M. M., McConnell, J. R., Murphy, L. N., Chellman, N., Das, S., Kipfstuhl, S., & Mulvaney, R. Holocene
795 black carbon in Antarctica paralleled Southern Hemisphere climate. *Journal of Geophysical Research: Atmospheres*,
796 **122**, 6713-6728 (2017).
797
- 798 60. Fudge, T. J., Markle, B. R., Cuffey, K. M., Buizert, C., Taylor, K. C., Steig, E. J., Waddington, E. D., Conway,
799 H., & Koutnik, M. Variable relationship between accumulation and temperature in West Antarctica for the past 31
800 000 years, *Geophys. Res. Lett.*, **43**, 3795–3803 (2016).
801
- 802 61. Casado, M., Münch, T., & Laepple, T. Climatic information archived in ice cores: impact of intermittency and
803 diffusion on the recorded isotopic signal in Antarctica. *Climate of the Past*, **16**, 1581-1598 (2020).
804
- 805 62. Hwang, Y. T. & Frierson, D. M. Increasing atmospheric poleward energy transport with global warming.
806 *Geophysical Research Letters*, **37**, (2010).
807
- 808 63. Roe, G. H., Feldl, N., Armour, K. C., Hwang, Y. T., & Frierson, D. M. The remote impacts of climate feedbacks
809 on regional climate predictability. *Nature Geoscience*, **8**, 135-139 (2015).
810
- 811 64. Siler, N., Roe, G. H., & Armour, K. C. Insights into the zonal-mean response of the hydrologic cycle to global
812 warming from a diffusive energy balance model. *Journal of Climate*, **31**, 7481-7493 (2018).
813
- 814 65. Gordon, C., Cooper, C., Senior, C. A., Banks, H., Gregory, J. M., Johns, T. C., Mitchell, J. F. & Wood, R. A. The
815 simulation of SST, sea ice extents and ocean heat transports in a version of the Hadley Centre coupled model without
816 flux adjustments. *Climate dynamics*, **16**, 147-168 (2000).
817
- 818 66. Valdes, P. J., Armstrong, E., Badger, M. P. S., Bradshaw, C. D., Bragg, F., Crucifix, M., Davies-Barnard, T., Day,
819 J. J., Farnsworth, A., Gordon, C., Hopcroft, P. O., Kennedy, A. T., Lord, N. S., Lunt, D. J., Marzocchi, A., Parry, L.
820 M., Pope, V., Roberts, W. H. G., Stone, E. J., Tourte, G. J. L., & Williams, J. H. T. The BRIDGE HadCM3 family of
821 climate models: HadCM3@Bristol v1.0, *Geosci. Model Dev.*, **10**, 3715–3743 (2017).
822
- 823 67. DiNezio, P. N. & Tierney, J. E. The effect of sea level on glacial Indo-Pacific climate. *Nature Geoscience*, **6**, 485–
824 491 (2013).
825
- 826 68. Berger, A. & Loutre, M. F. Insolation values for the climate of the last 10 million years. *Quaternary Science*
827 *Reviews*, **10**, 297–317 (1991).
828

- 829 69. Spahni, R., Chappellaz, J., Stocker, T. F., Loulergue, L., Hausammann, G., Kawamura, K., Flückiger, J.,
830 Schwander, J., Raynaud, D., Masson-Delmotte, V. & Jouzel, J. Atmospheric methane and nitrous oxide of the late
831 Pleistocene from Antarctic ice cores. *Science*, **310**, 1317-1321 (2005).
832
- 833 70. Loulergue, L., Schilt, A., Spahni, R., Masson-Delmotte, V., Blunier, T., Lemieux, B., Barnola, J. M., Raynaud,
834 D., Stocker, T. F. & Chappellaz, J. Orbital and millennial-scale features of atmospheric CH₄ over the past 800,000
835 years. *Nature*, **453**. 383-386 (2008).
836
- 837 71. Peltier, W. R., Argus, D. F., & Drummond, R. Space geodesy constrains ice age terminal deglaciation: The global
838 ICE-6G_C (VM5a) model. *Journal of Geophysical Research: Solid Earth*, **120**, 450-487 (2015).
839
- 840 72. Tarasov, L. & Richard Peltier, W. Greenland glacial history and local geodynamic consequences. *Geophysical*
841 *Journal International*, **150**, 198-229 (2002).
842
- 843 73. Tarasov, L., Dyke, A. S., Neal, R. M., & Peltier, W. R. A data-calibrated distribution of deglacial chronologies for
844 the North American ice complex from glaciological modeling. *Earth and Planetary Science Letters*, **315**, 30-40
845 (2012).
846
- 847 74. Tarasov, L., Hughes, A., Gyllencreutz, R., Lohne, O. S., Mangerud, J., & Svendsen, J. I. The global GLAC-1c
848 deglaciation chronology, meltwater pulse 1-a, and a question of missing ice. *In IGS Symposium: Contribution of*
849 *Glaciers and Ice Sheets to Sea-Level Change, Chamonix, France, 26-30 (2014, May)*.
850
- 851 75. Abe-Ouchi, A., Saito, F., Kawamura, K., Raymo, M. E., Okuno, J. I., Takahashi, K., & Blatter, H. Insolation-
852 driven 100,000-year glacial cycles and hysteresis of ice-sheet volume. *Nature*, **500**, 190-193 (2013).
853
- 854 76. Steig, E. J., Huybers, K., Singh, H. A., Steiger, N. J., Ding, Q. H., Frierson, D. M. W., Popp, T., & White, J. W.
855 C. Influence of West Antarctic Ice Sheet collapse on Antarctic surface climate, *Geophys. Res. Lett.*, **42**, 4862–4868
856 (2015).
857

858
859
860
861
862
863
864
865
866
867
868
869
870
871
872
873
874
875
876
877
878
879
880
881
882
883
884
885
886
887
888
889
890
891
892

Acknowledgements

This work was supported by US National Science Foundation (NSF) grants 0537593, 0537661, 0537930, 0539232, 1043092, 1043167, 1043518, 1142166, and 1807478. Field and logistical activities were managed by the WAIS Divide Science Coordination Office at the Desert Research Institute, Reno, NE, USA and the University of New Hampshire, USA (NSF grants 0230396, 0440817, 0944266, and 0944348). The National Science Foundation Division of Polar Programs funded the Ice Drilling Program Office (IDPO), the Ice Drilling Design and Operations (IDDO) group, the National Ice Core Laboratory (NICL), the Antarctic Support Contractor, and the 109th New York Air National Guard. K.M.C.'s work was supported by The Martin Family Foundation. W.H.G.R. was funded by a Leverhulme Trust Research Project Grant. HadCM3 simulations were carried out using the computational facilities of the Advanced Computing Research Centre, University of Bristol - <http://www.bris.ac.uk/acrc/> and Oswald, University of Northumbria. We thank Cécile Agosta for providing the MAR outputs. We thank the Stable Isotope Lab at INSTAAR for their expertise in helping to measure the water isotope data sets used in this study.

Author Contributions

T.R.J. designed the project. T.R.J. K.M.C., and W.H.G.R. led the writing of the paper, with help from B.R.M. and E.J.S. High-resolution water isotope measurements were contributed by T.R.J. and J.W.C.W., the analysis of the water isotopes was led by V.M., B.H.V., T.R.J., and J.W.C.W. HadCM3 simulations were conducted by W.H.G.R. and P.J.V., while W.H.G.R. developed the methodology for determining how modeled sea ice affects West Antarctic temperature. B.R.M. conducted MEBM simulations. C.M.S. and T.R.J. conducted CFM simulations. T.R.J., K.M.C., and B.M.V. developed the diffusion-correction calculations, with help from A.G.H., and C.A.B. T.R.J. developed the methodology for the selection of extrema (summer and winter) in the diffusion-corrected water isotope data. T.R.J. developed the methodology for quantifying the effect of seasonal accumulation on water-isotope diffusion using the CFM and chemistry data. T.R.J. and K.M.C. determined the methodology for the uncertainty of seasonal temperature reconstruction. K.M.C. and E.J.S. determined the methodology for the uncertainty of multi-millennial temperature trends, with help from T.R.J. B.R.M. provided isotope-temperature scaling uncertainty using SWIM. K.M.C. determined the methodology for constraints on WAIS Divide elevation changes in the Holocene. T.J.F. and M.S. provided chemistry data. T.R.J., V.M., B.H.V., J.G., and K.S.R. assisted with the development of the water isotope dataset over depths of 1035.4 to 1368.2 m. All authors discussed the results and contributed input to the manuscript.

Author Information

Reprints and permissions information is available at www.nature.com/reprints. The authors declare no competing financial interests. Readers are welcome to comment on the online version of the paper. Correspondence and requests for materials should be addressed to T.R.J. (tyler.jones@colorado.edu).

Month	\bar{b} (m ice eq. yr ⁻¹)	σ_b (m ice eq. yr ⁻¹)	T (°C)	δD (‰)
1	0.139	0.088	-17.5	-250.22
2	0.169	0.072	-24.9	-252.48
3	0.267	0.010	-31.5	-258.64
4	0.293	0.121	-34.6	-267.05
5	0.345	0.137	-34.9	-275.46
6	0.311	0.136	-36.2	-281.61
7	0.310	0.111	-38.1	-283.87
8	0.298	0.116	-38.6	-281.61
9	0.275	0.112	-37.1	-275.46
10	0.271	0.136	-31.6	-267.05
11	0.164	0.079	-23.8	-258.64
12	0.128	0.071	-17.3	-252.48

893
894
895
896
897

ED Table 1 | CFM simulation inputs. Mean \bar{b} and standard deviation σ_b of each month's accumulation rate and monthly mean temperature at WAIS Divide for 1979 to 2017 predicted by MAR⁵⁶ and the isotope values used for each month during the CFM simulations.

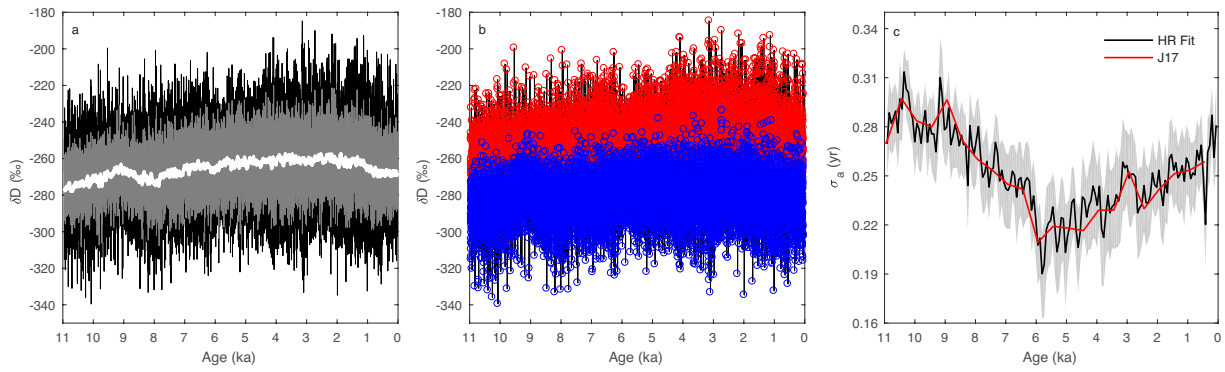
11-0 ka	1,000-year averages	300-year averages	300 to 1,000-year residuals
Summer vs. mean	0.87	0.82	0.26
Winter vs. mean	0.40	0.37	0.31

11-7 ka	1,000-year averages	300-year averages	300 to 1,000-year residuals
Summer vs. mean	0.7	0.49	0.01
Winter vs. mean	0.54	0.62	0.74

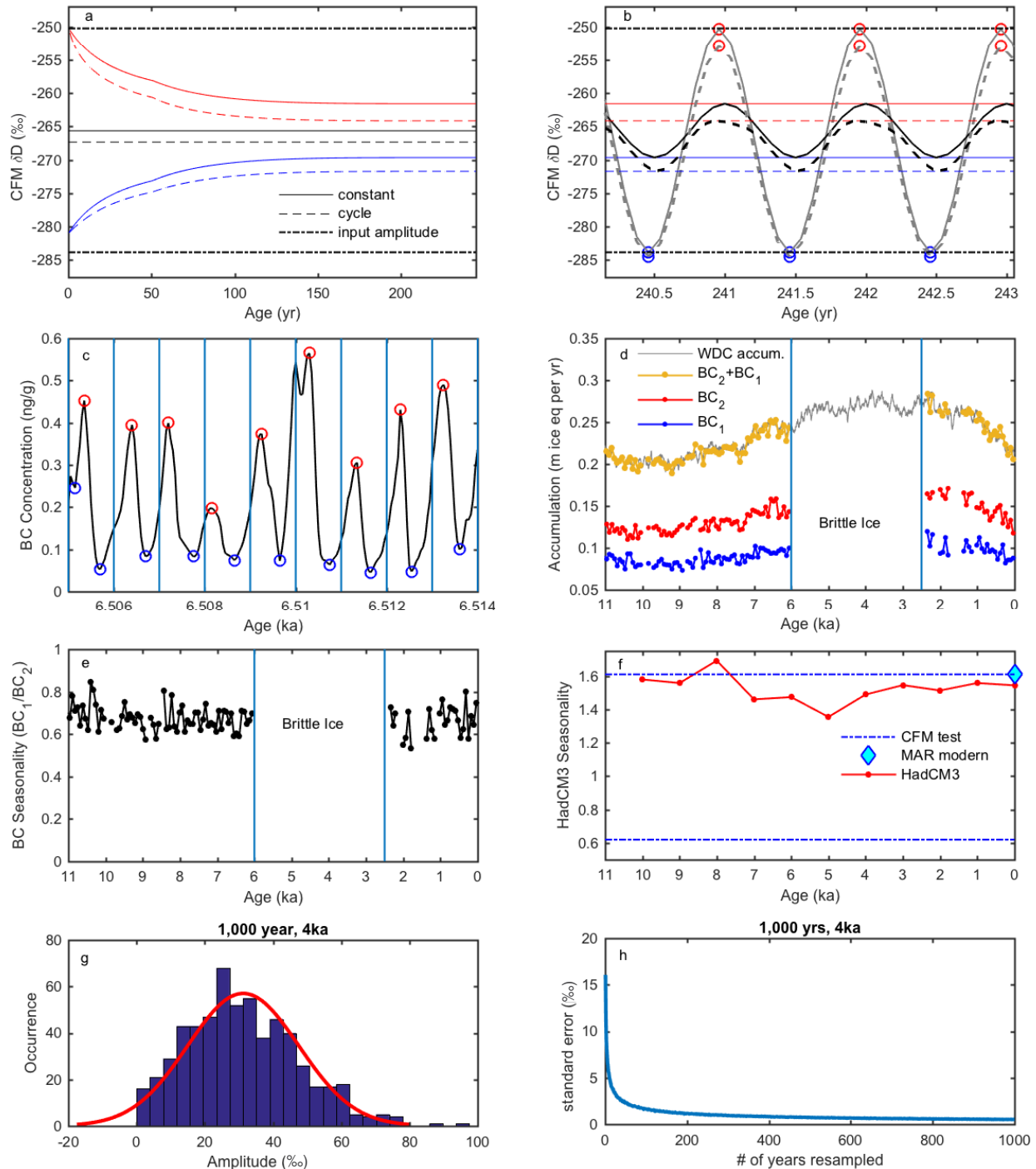
898
899 **ED Table 2 | Seasonal vs. mean correlations.** R^2 values for 1,000-year and 300-year averages of summer and winter
900 vs. mean, as well as for residuals.
901

	SST	Sea ice	TOA insolation
Control	0ka	0ka	0ka
Atmos_10k	10ka	10ka	10ka
Atmos_10k_ice/SST	10ka	10ka	0ka
Atmos_10k_insol	0ka	0ka	10ka
Atmos_10k_ice	0ka	10ka	0ka
Atmos_10k_SST	10k	0ka	0ka

902
903 **ED Table 3 | Atmosphere-only climate model experiments.** Variations of boundary conditions in each experiment.
904

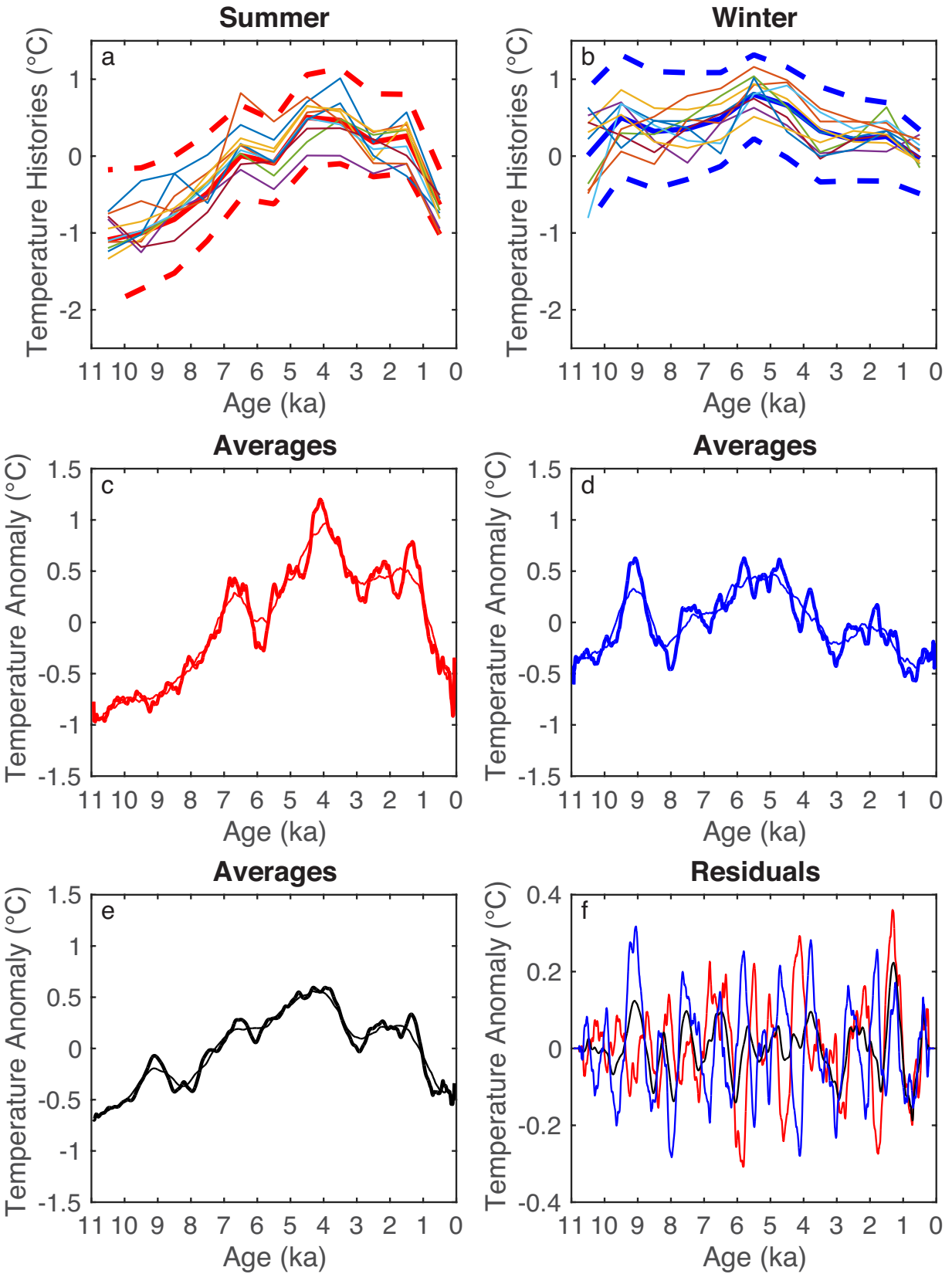


905
 906 **ED Figure 1 | WDC water-isotope data.** *a*, The raw, high-resolution WDC δD water isotope record^{18,19,20} (grey), the
 907 raw 50-yr running mean (white), and the diffusion-corrected signal (black). *b*, The WDC diffusion-corrected δD
 908 record with extrema picks for summer (red) and winter (blue). *c*, The high-resolution diffusion length record (black;
 909 140-yr windows, 70-yr time steps; 1σ uncertainty bounds in light grey) compared to prior estimates²⁶ (red; 500-yr
 910 windows, 500-yr time steps).
 911



912 **ED Figure 2 | Precipitation uncertainties.** Uncertainties for seasonally weighted accumulation are shown in a-f,
 913 and for precipitation intermittency in g-h. **a**, The diffusion envelope of CFM output data (50-yr avg.), based on an
 914 input sine wave with $f=1\text{yr}^{-1}$ and amplitude=15.43%. The original amplitude of the signal (based on the dotted dashed
 915 lines) decreases as time passes due to downward advection of the firm, as shown by the decay of the maximum (red)
 916 and minimum (blue) lines, while the mean values of the ‘constant’ and ‘cycle’ scenarios do not change, dependent on
 917 the seasonal weighting of snowfall. **b**, Diffused CFM output data from beneath the pore close-off depth (>200 yr)
 918 (black lines; smaller amplitude), with diffusion-corrected data shown with grey lines (larger amplitude). Red circles
 919 are the annual maximum value, and blue circles the annual minimum, selected using the same algorithm as Figure
 920 1a. **c**, A zoom of black carbon concentrations at $\sim 6.5\text{ ka}^{57}$. The maxima (red circles) and minima (blue circles) can be
 921

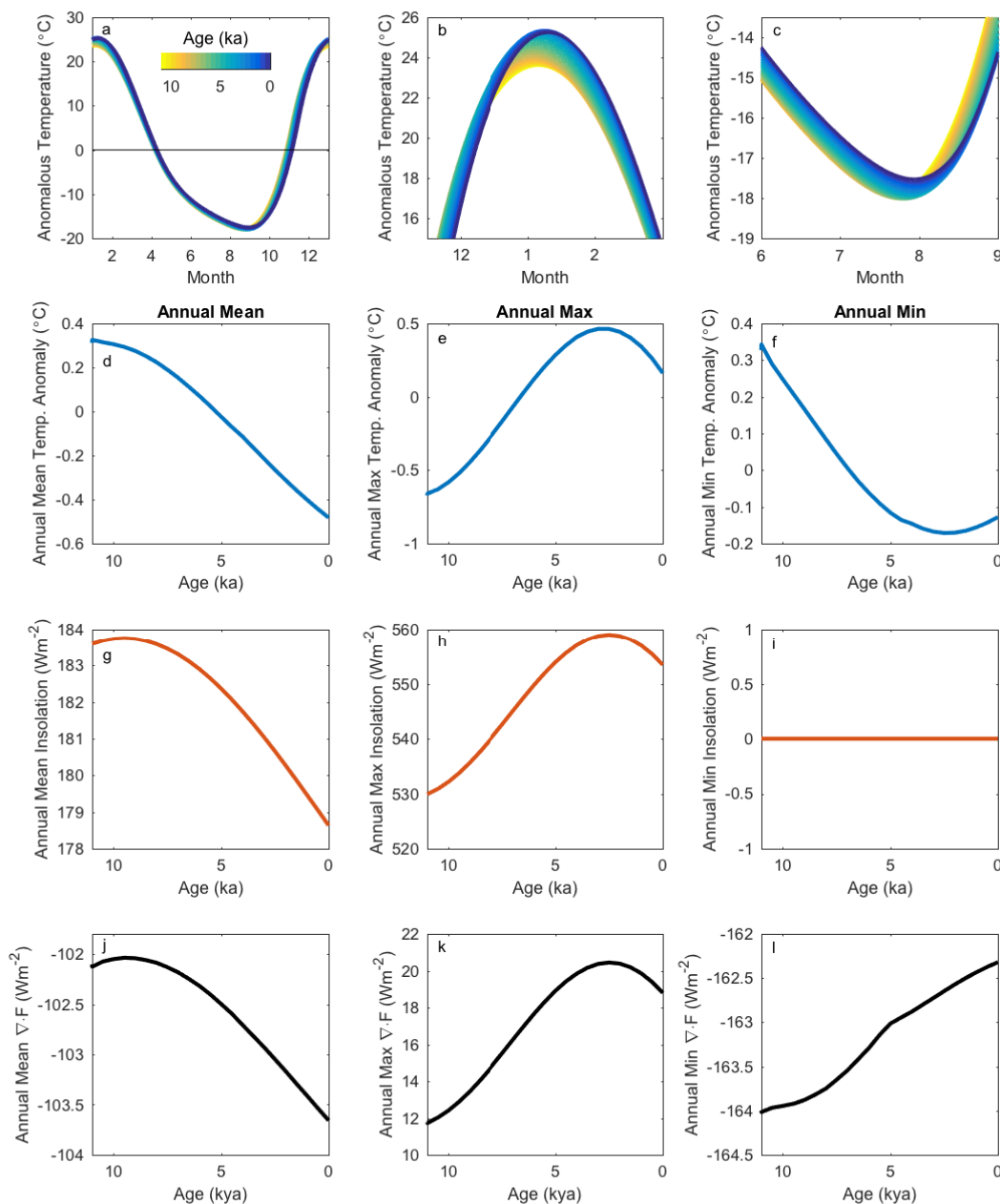
922 used to separate approximate depth intervals corresponding to winter (BC_1) and summer (BC_2); vertical blue lines
923 correspond to nominal January 1, as defined by the peak of $nssS/Na^{22}$. **d**, The 140-yr averages for BC_1 (blue) and BC_2
924 (red). The grey line is WDC annual accumulation⁶⁰, orange circles are $BC_1 + BC_2$, which should equal annual
925 accumulation. **e**, Black carbon seasonality BC_1/BC_2 (black), based on (d). **f**, Accumulation seasonality for HadCM3
926 seasonal snowfall (red line) compared to the range of seasonality tested using the CFM (dashed blue lines) and
927 modern MAR seasonality⁵⁸ (blue diamond). **g**, Distribution of annual amplitudes for water isotopes for a 1,000-year
928 window centered at 4 ka. **h**, Standard errors are determined for 1,000-realizations of random sampling of the
929 distribution in (a) to determine a standard deviation of the residuals of the true mean minus the mean of the random
930 sampling.
931



932
933

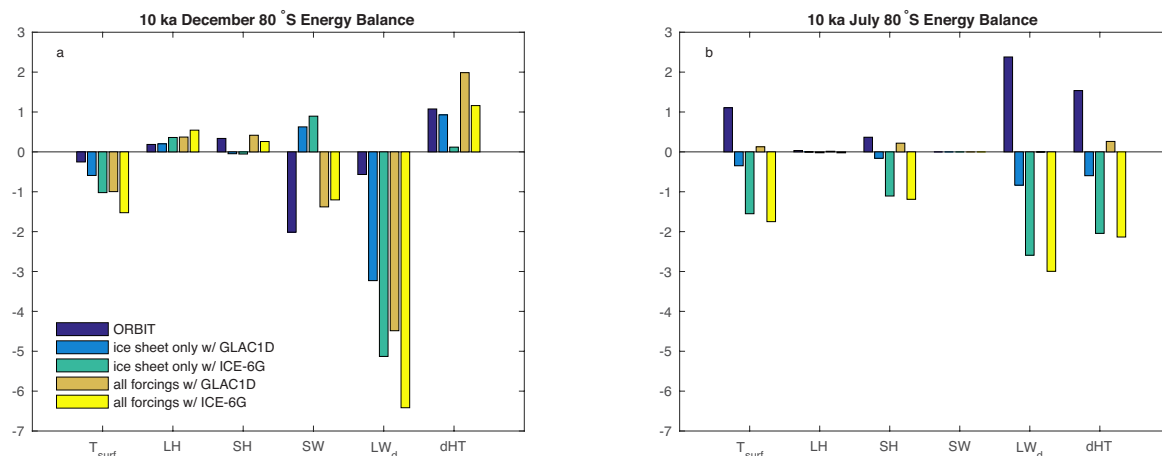
ED Figure 3 | Trend analysis. *a,b*, The first 10 of 10,000 randomly generated, alternative seasonal temperature

934 histories for summer (a) and winter (b), used in Figure 2b,d to generate probability distributions of temperature trends
 935 in the Holocene. Thick, solid lines are mean values, and thick, dashed lines are 2σ uncertainty ranges. c-f, The 1,000-
 936 year (thin line) and 300-year (thick line) averages normalized to the 11-0 ka mean (c-e) and residuals (1,000 year
 937 minus 300 year) (f) of summer (red), winter (blue), and the mean (black), used to calculate R^2 values in ED Table 2.
 938

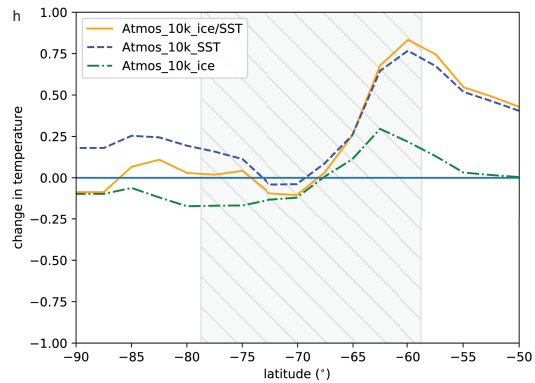
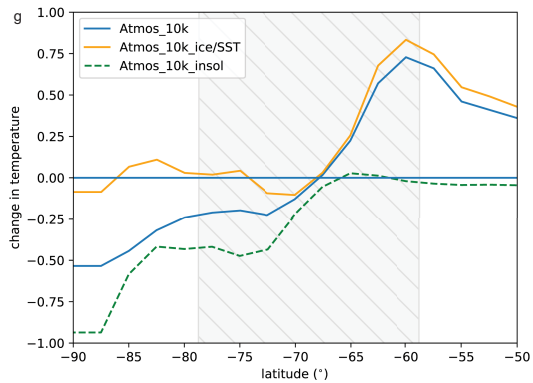
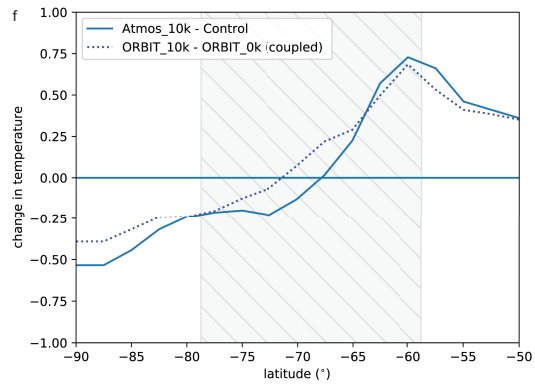
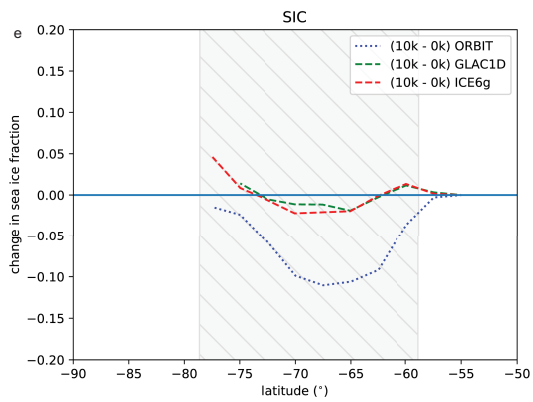
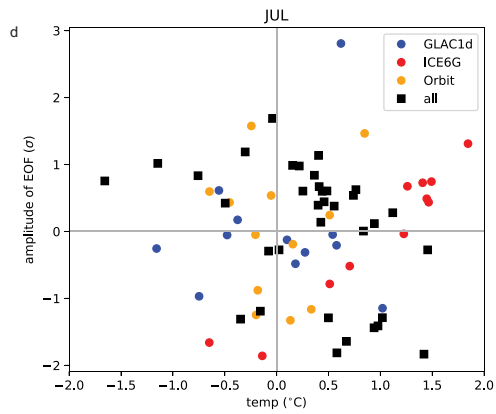
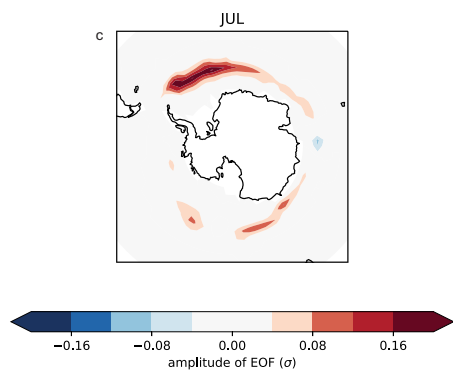
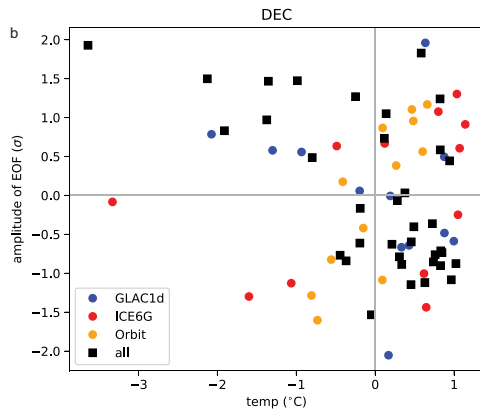
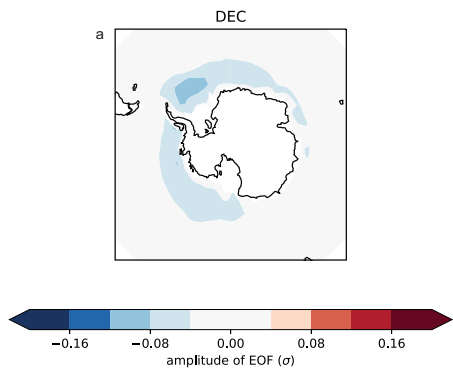


939 **ED Figure 4 | MEBM results.** MEBM seasonal surface temperatures are shown in a-c. a, Modeled seasonal surface
 940 temperature cycle at 80°S, colored by age. b, c, Zoom in of modeled summer and winter temperature. MEBM annual
 941 results for the mean, maximum, and minimum are shown in d-l. Plots for temperature anomaly normalized to the
 942

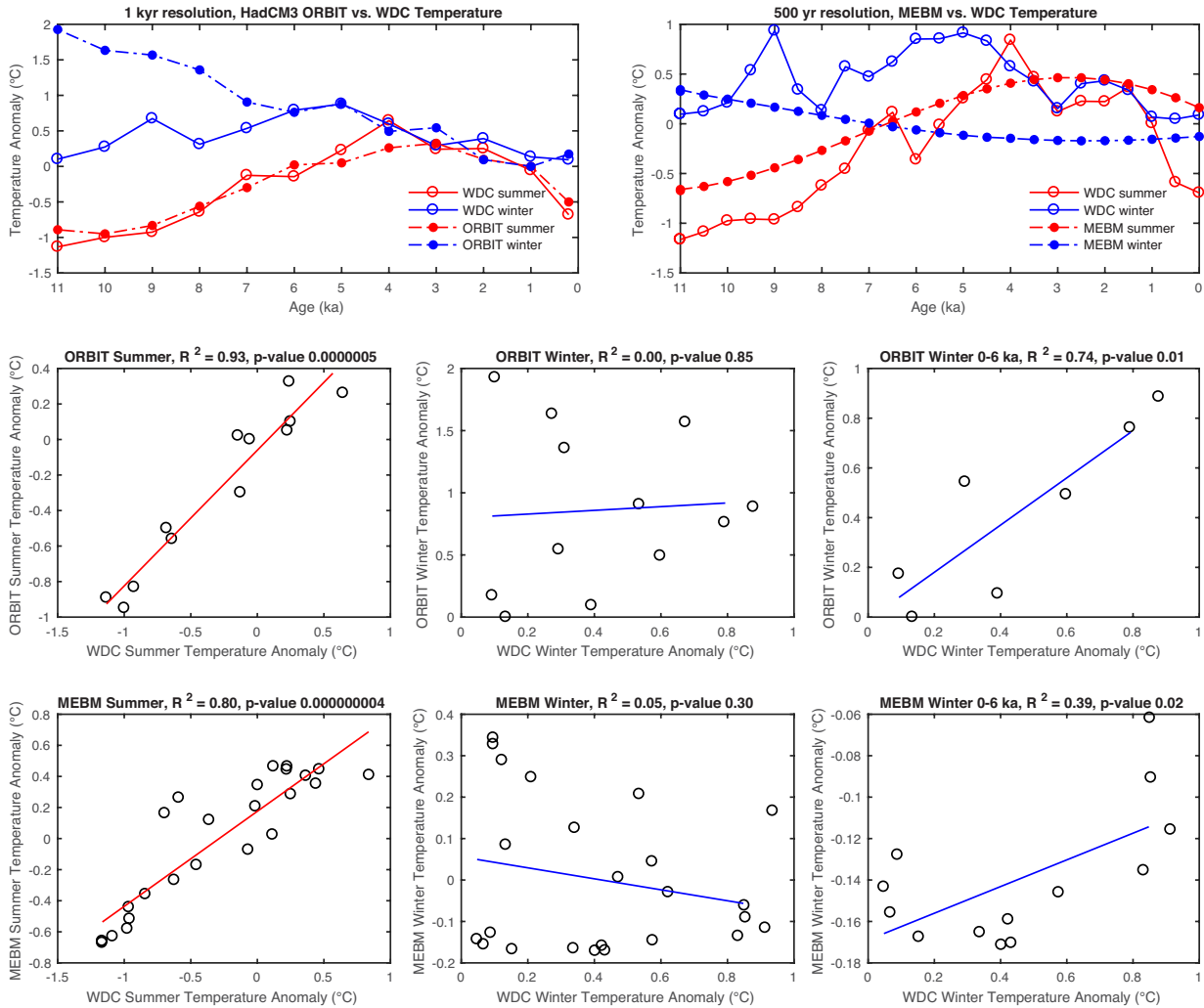
943 mean (blue), insolation (red), and heat divergence (black) for the annual mean (d-f), annual max (g-i), and annual
 944 min (j-l). Note the sign of heat divergence; negative values correspond to heat convergence at the site.
 945



946
 947 **ED Figure 5 | 80°S energy balance at 10 ka.** Bar charts of HadCM3 energy balance terms at 10 ka for **a**, December
 948 (summer) and **b**, July (winter), including model runs for ‘orbit only’ (purple, ORBIT), ‘ice sheet only’ (blue, GLAC1D;
 949 green, ICE-6G), and ‘all forcings’ (orange, GLAC1D; yellow, ICE-6G). Positive values all indicate a surface or
 950 atmospheric warming. Variables include surface temperature (T_{surf} in °K), latent heat (LH in Wm^{-2}), sensible heat to
 951 the surface (SH_d in Wm^{-2}), shortwave radiation (SW in Wm^{-2}), downward LW radiation (LW_d in Wm^{-2}), and change in
 952 heat transport ($\nabla \cdot \mathbf{F}$ in $10^7 W$).
 953



955 **ED Figure 6 | Sea ice variability and temperature in HadCM3 simulations.** Maps of the dominant pattern of
 956 variability in each of the seasons and scatter plots of amplitude of the pattern against temperature. Maps were created
 957 using Python's package cartopy. **a,c**, The EOF of sea-ice variability in the Southern Hemisphere for December and
 958 July in ALL of the simulations: this is the dominant pattern of sea ice variability. **b,d**, The amplitude of the patterns in
 959 (a) and (c) vs. the temperature at 80°S for each simulation. Plots e-h show the zonal mean temperature and sea ice in
 960 HadCM3 simulations for December average. **e**, Change in sea-ice fraction for coupled-model simulations from 10k
 961 to 0k. **f**, Change in surface temperature between 10k and 0k for the coupled-model simulations (dotted line) and
 962 atmosphere-only simulations (solid line). **g**, Change in surface temperature for atmosphere-only runs from 10k to 0k.
 963 **h**, Change in surface temperature for atmosphere-only runs from 10k to 0k. See ED Table 3 for descriptions of the
 964 model simulations used in panels (g) and (h).
 965



966 **ED Figure 7 | Model results vs. WDC temperatures.** Coefficient of determination and p-values for comparison of
 967 HadCM3 (1-kyr resolution, $n=12$) or MEBM (0.5-kyr resolution, $n=23$) model results with WDC summer and winter
 968 temperatures.
 969